A Toy Model of the Madden-Julian Oscillation

Ian Folkins (Department of Physics and Atmospheric Science, Dalhousie University)
Email: ian.folkins@dal.ca

We discuss a simple three layer model of the tropical atmosphere. The rainfall variance of the model is dominated by a rainfall mode moving parallel to the equator having the approximate size and propagation speed of the Madden-Julian Oscillation (MJO). The origin of the convective aggregation in the model is the imposition of distinct length scales for the deep updraft and stratiform downdraft circulations. Subsidence induced by the deep updraft circulation suppresses convective instability on a scale of ~ 1000 km, while ascent induced by the downdraft circulation promotes convective instability on a scale of ~ 500 km. Within the MJO envelope, high rainfall rates are maintained both by increased column relative humidity, and increased variance in lower tropospheric vertical motion. Each of the three model layers has a prescribed target pressure thickness. Convective mass fluxes introduce a mass excess into grid cells where there is net detrainment, and a mass deficit into grid cells from which there is net entrainment. Horizontal transport in the model is based on export of mass from grid cells where there is an excess, and import of mass toward grid cells where there is a deficit. The resulting patterns of horizontal convergence and divergence generate vertical motions between model levels. The simulated MJO events propagate eastward when there is a slight preference for mass deficits in the boundary layer to be compensated by inward flow from the west. The forward propagation of the MJO is limited by the rate at which the downdraft circulation within the MJO is able to generate net upward motion and promote new convective activity in advance of the leading edge. We also offer some guidance on how convective parameterizations that are implemented in models with more realistic dynamical schemes might be designed to exhibit stronger MJO variance.

1. Introduction

The Madden-Julian Oscillation (MJO) is an important mode of tropical rain variance. However, there does not appear to be any simple, widely accepted explanation of its origin, size, propagation direction, or propagation speed (Zhang et al. 2020). The lack of such an explanation has impeded attempts to simulate the MJO in climate and weather forecast models (Hung et al. 2013; Ren et al. 2021). We present a simple explanation of the origin of the MJO using a three layer model of the tropical troposphere. The model is not directly based on the dynamical equations of motion, but is intended to provide conceptual guidance on how models with more realistic dynamics might be integrated with convective parameterizations to generate increased MJO rainfall variance.

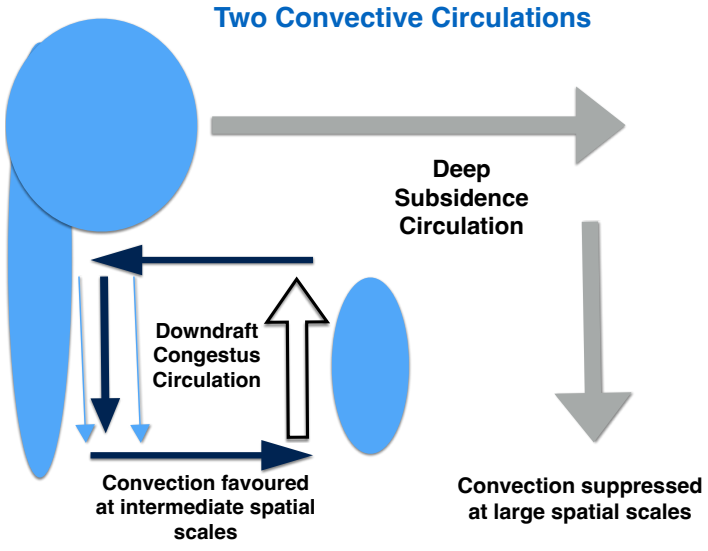

FIG. 1: Overview of the two main convective circulations in the tropics. Deep convective updrafts drive a large scale overturning circulation in which subsidence warming and drying inhibit convective development on the scale of several thousand km. Some of the precipitation falling from stratiform anvil clouds evaporates in the cloud free air below cloud base, generating downdrafts and induced ascent at intermediate spatial scales, and favoring the development of congestus clouds.

The explanation for the origin of the MJO advanced here is illustrated in Figure 1. Because of the large vertical depth of deep convective heating, and proximity to the equator where the Coriolis parameter is near zero, the deep convective Rossby radius in the tropics is on the order of several thousand km. The subsidence induced by deep convective detrainment occurs on a similar spatial scale, so that deep convection in the tropics gives rise to very large scale overturning circulations. Subsidence inhibits convective development by decreasing the relative humidity of the background atmosphere. Deep subsidence therefore contributes to an effective repulsion between deep convective cells, and a tendency to become as widely spaced from each another

as possible. This would result in a near uniform rainfall distribution in the tropics, provided the overall thermodynamic sources of convective instability, such as sea surface temperature, and the dynamical triggers for convective development, were also uniformally distributed. The convective clustering observed within an MJO therefore requires some mechanism by which deep convection increases convective instability on intermediate spatial scales.

This mechanism is provided by the downdraft congestus circulation. The injection of water and ice condensate into the upper troposphere by deep convective clouds gives rise to stratiform anvils which have a much larger spatial scale than the deep convective updrafts themselves. Precipitation falling from these anvil clouds typically falls through unsaturated cloud free air below the melting level, and generates stratiform downdrafts whose mass flux can be comparable to the updraft convective mass flux. The vertical depth of downdraft evaporative cooling ($\sim$ 4 km) is much smaller than the vertical depth of deep convective heating ($\sim$ 14 km). The spatial scale of the circulations generated by downdraft cooling can therefore be expected to be at least two times smaller than the circulations generated by deep updraft heating. The induced environment uplift generated by stratiform anvil downdrafts therefore occurs at an intermediate spatial scale, relative to the large scale descent induced by deep convection. Some of this induced ascent would be expected to favor the development of cumulus congestus clouds (Johnson et al. 1999), which, because of their smaller size, lack of internal organization, and short lifetimes (Waite and Khouider 2010) can be expected to be nearly in phase with the upward motion of the background atmosphere. To the extent that congestus clouds moisten the lower troposphere and serve as potential sites for the development of deep convection, they would act in concert with the induced downdraft uplift to favor the development of subsequent deep convection (Mapes 1993). The downdraft congestus circulation shown in Figure 1 could therefore provide the required mechanism for convective aggregation on the spatial scale of an MJO.

The explanation for the convective clustering observed in the MJO given in the previous paragraph is intuitively quite simple. However, the implementation of this mechanism in a model is not straightforward. The spatial and temporal scales of the MJO require that such models simulate the entire tropics. Convection resolving models of this scale are very computer intensive, and still require parameterizations of turbulence, radiation, and microphysical processes (Guichard and Couvreux 2017). Most models attempting to simulate the MJO have therefore relied on

convective parameterizations. However, there are significant uncertainties in how to parameterize deep convection, cumulus convection, downdrafts, and stratiform anvil processes, and how to couple the convective mass fluxes generated by the parameterization with the grid scale variables of the model. In addition, the initial phase of dynamical adjustment to a heat source is mediated by waves (Mapes 1993). Models may not always resolve the waves generated by convective heat sources with sufficient accuracy to simulate the smaller scale downdraft congestus circulation, even if the magnitude of this heat source is correctly simulated by the convective parameterization. Here, we implement the two convective circulations MJO mechanism in a very simple three layer model of the tropics. The model has parameterizations for deep convection, which transports mass from the boundary layer to the upper troposphere, for cumulus convection, which transport mass from the boundary layer to the lower troposphere, and for downdrafts, which transport mass from the lower troposphere to the boundary layer. The effect of horizontal transport is to smooth out the mass anomalies generated in various grid cells by the vertical convective mass fluxes. In effect, it imposes by fiat the horizontal motions that would be expected from the wave mediated response to convective heat sources. For the upper troposphere and boundary layers of the model, the horizontal transport occurs over a spatial scale comparable to the Rossby radius of the deep convective circulation. For the lower tropospheric layer, it occurs over a spatial scale comparable to the Rossby radius of the downdraft congestus circulation. The model also has parameterizations for radiative descent, and for vertical motions forced by a difference in horizontal mass divergence between two levels.

Section 2 gives brief descriptions of the three datasets used to assess the model performance. In Section 3, we argue that the actual horizontal length scales of the downdraft congestus and deep updraft circulations are smaller than would be implied by the theoretical expressions for their Rossby radii based on the depth of their respective heat sources. The fourth section is a technical description of the main model components. Although the model is quite simple in principle, there are some subtleties associated with the implementation of horizontal transport, due to the requirement that the length scales of the two convective circulations vary as a function of latitude. In Section 5, we discuss the main results of the default version of the model. These include the multiscale structure of the simulated MJO events, the internal circulation within an MJO which gives rise to symmetric congestus lobes on both sides of the equator, and the surface

pressure pattern which is consistent with a westerly inflow toward the MJO from the trailing western edge. We also assess the realism of the simulated interaction between the background vertical motion and the convective mass fluxes, through comparison with the growth and decay of observed mass divergence profiles about high rain events in the Western Tropical Pacific. We then compare the spectral strength of the simulated MJO variance with the observed MJO variance. The eastward zonal speed of the simulated MJO events in the default version of the model is roughly 6 m/s. Somewhat surprisingly, it is difficult to find model parameters which significantly change this speed, without at the same time also destroying the simulated MJO variance. We derive a diagnostic expression for the MJO propagation speed based on the simulated rate of deep convective mass production just in front of the leading eastern edge of the MJO. In Section 6, we modify various parameters to help determine which model processes are essential to the simulation of the MJO, and which determine the direction of zonal propagation. Section 7 is a discussion of some of the technical difficulties that can be encountered in attempting to couple the convective mass fluxes generated by the convective parameterization of a large scale model to the background vertical motion. Section 8 discusses the main results and limitations of the model.

2. Datasets

The Tropical Rainfall Measuring Mission (TRMM) obtained rainfall estimates from five instruments on the TRMM satellite in combination with other satellite and rain gauge measurements (Huffman et al. 2012). The 3B42 TRMM rainfall dataset used here has a spatial resolution of 0.25^{o}, a time step of 3 hours, and extends from 50 ^{o}S to 50 ^{o}N.

The Integrated Global Radiosonde Archive (IGRA) is produced by the National Climatic Data Center (NCDC) (Durre et al. 2006). We used twice daily wind data from 1998 to 2008 from six IGRA radiosonde stations near the equator, on the standard pressure levels of 1000, 925, 850, 700, 500, 400, 300, 250, 200, 150, and 100 hPa.

We also used radiosonde data at five stations from the United States High Vertical Resolution Radiosonde Data (HVRRD) archive. The five stations used here are Koror (Palau Island: 7.33 ^{o}N, 134.48^{o}E), Yap Island (9.48 ^{o}N, 138.08 ^{o}E). Truk (Moen Island: 7.47 ^{o}N, 151.85 ^{o}E), Ponape Island (6.97 ^{o}N, 158.22 ^{o}E), and Majuro (Marshall Island: 7.08 ^{o}N, 171.38 ^{o}E). The temperature

anomaly of an individual radiosonde profile was defined with respect to monthly mean temperature profiles on a 200 m vertical grid.

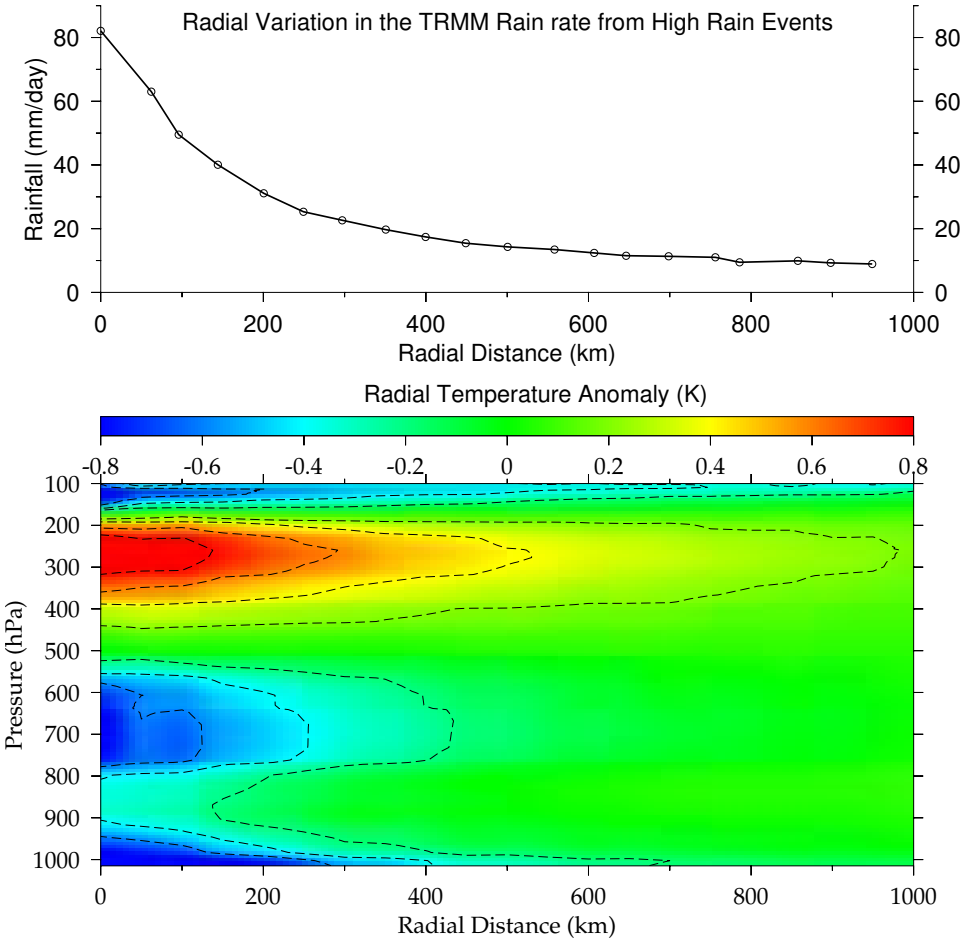

FIG. 2: The trimodal temperature response to tropical deep convection: upper tropospheric warming (450 hPa - 150 hPa), lower tropospheric cooling (800 hPa - 500 hPa), and boundary layer cooling (below 900 hPa). Deep convection also cools the Tropical Tropopause Layer (150 hPa - 80 hPa). This temperature anomaly response pattern has motivated the choice of an upper tropospheric horizontal length scale $L_{UT} \sim 1100$ km, and lower tropospheric length scale $L_{LT} \sim 500$ km, near the equator.

3. Trimodal temperature response to deep convection

The ratio between the updraft and downdraft mass fluxes within a deep convective system is likely to be strongly height dependent. However, model simulations suggest that the downdraft mass flux is on the order of one half of the updraft mass flux (Windmiller et al. 2023). The convective feedback mechanism shown in Figure 1 therefore requires that the induced uplift from deep stratiform downdrafts be distributed over a substantially smaller area than the induced descent

from the deep updrafts. Some indication of the relative spatial size of the downdraft and deep updraft circulations can be obtained from the radial distribution of the temperature response to strong convective events shown in Figure 2. This figure was adapted from an earlier publication (Folkins 2013), and was obtained by first averaging the TRMM rain rates over larger 0.5^o latitude x 0.625^o longitude grid boxes. We then looked for grid boxes where the TRMM rain rate within any 3 hour interval exceeded 36 mm day^{-1}. If the radial distance of the rain event from one of the five Western Pacific HVRRD radiosonde stations discussed above was less than 1000 km, and the launch time of the radiosonde occurred within the 3 hour time window of the TRMM rainfall event, we calculated the radiosonde temperature anomaly profile with respect to the monthly mean temperature profile at that location. The temperature anomaly profiles of the five radiosonde stations were then combined with the relative distance from each rain event to construct the composite temperature response pattern shown in the lower plot of Figure 2. The upper plot of Figure 2 shows the the radial variation in the mean rainfall rate, averaged over all rain events.

Figure 2 shows that tropospheric temperature response to deep convection has three distinct layers: cooling near the surface (below 900 hPa), cooling in the lower troposphere (800 hPa - 550 hPa), and warming in the upper troposphere (450 hPa – 150 hPa) (Sherwood and Wahrlich 1999; Mapes et al. 2006; Mitovski et al. 2010; Virman et al. 2020). This temperature response pattern results in the development of a positive stability anomaly near the melting level, and is associated with the preferential development of cumulus congestus clouds (Bister and Mapes 2004). The use of a three layer model in this paper is partially motivated by the trimodal temperature response pattern shown in this figure. Higher rates of convective rainfall also give rise to a cooling in the tropical tropopause layer (150 hPa - 80 hPa). The near surface cooling can presumably be attributed to some combination of preferential entrainment of warmer air into deep convective updrafts, together with the injection of evaporatively cooled air into the boundary layer from the more strongly negatively buoyant downdrafts that are generated by higher rates of convective precipitation. The existence of two distinct downdraft cooling maxima is consistent with model simulations showing a distinct peak in downdraft mass flux just below the melting level at 3.7 km, and another peak near the top of the boundary layer at 1.5 km (Windmiller et al. 2023).

The lower panel of Figure 2 shows that the length scales of the upper tropospheric warming and lower tropospheric cooling are roughly 1000 km and 500 km, respectively. The Rossby radius of

deformation L_{RR} associated with a heat source of vertical depth H, in an atmosphere with a Brunt Väisälä frequency N, at a latitude with Coriolis frequency f, is given by

$$L_{RR} = NH/f. \tag{1}$$

From the lower panel of Figure 2, the lower tropospheric cooling extends from 800 hPa to 550 hPa. Using the climatological variation of pressure and potential temperature with height at the five HVRRD radiosonde stations used to construct Figure 2, it can be shown that $N \sim 0.013\ s^{-1}$ and $H \sim 3100$ m. Use of the Coriolis frequency appropriate for a mean latitude of roughly 7^{o} in Eq. (1) gives $L_{RR} \sim 2000$ km. This theoretical estimate is considerably larger than the stratiform downdraft cooling circulation length scale indicated from Figure 2. This discrepancy may be partly related to the increased relative importance of dissipation near the equator, where the Rossby radius would otherwise become infinite. It is also possible that, on the timescales comparable with downdraft formation and subsequent wave generation, stratiform downdraft cooling rates are more stochastic, and have an effectively smaller vertical extent, than the $H \sim 3100$ m implied here from Figure 2. Whatever the reason, we will subsequently assume that the most appropriate length scales for the deep updraft and downdraft circulations near the equator are those inferred from Figure 2, rather than the theoretical estimates based on the vertical depths of their heating profiles given in Eq. (1).

4. Model description

a. Overall structure

The model was restricted to within 30^{o} of the equator. The horizontal resolution was 1.5^{o} in both longitude and latitude directions. The time step was 60 minutes. As shown in Figure 3, sea surface temperatures were fixed at 29 ^{o}C at the equator, decreasing with distance from the equator in a Gaussian manner to reach 23 ^{o}C at the northern and southern model boundaries. The three layers of the model were referred to as the boundary layer (BL), lower troposphere (LT), and upper troposphere (UT). The mass, or pressure difference, of the grid cells of a layer were permitted to vary in response to vertical or horizontal mass fluxes. However, grid cells in the boundary layer, lower troposphere, and upper troposphere were assigned target pressure difference of 100 hPa ($\Delta p_{BL,tar} = 100$ hPa), 400 hPa ($\Delta p_{LT,tar} = 400$ hPa), and 350 hPa ($\Delta p_{UT,tar} = 350$ hPa),

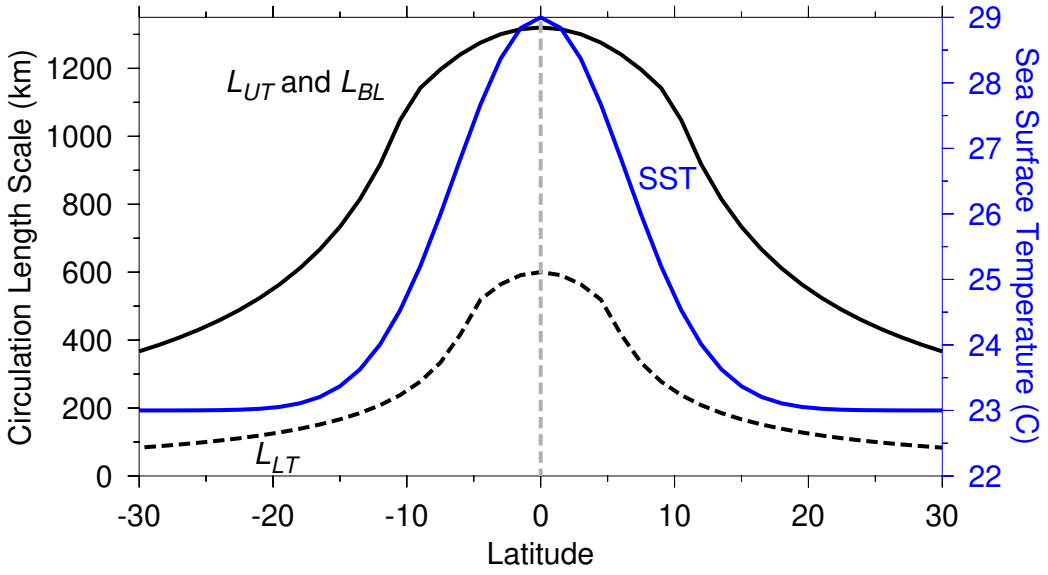

FIG. 3: The solid black curve shows the prescribed latitudinal variation of the length scale for horizontal transport for the upper tropospheric and boundary layers of the model (L_{UT} and L_{BL}). It is therefore the spatial scale of the deep circulation. The dashed black curve shows the length scale for horizontal transport of the lower troposphere L_{LT}, and defines the spatial scale of the downdraft congestus circulation. The blue curve shows shows the latitudinal variation of the sea surface temperature.

respectively. The pressure at the top of the model was considered to be 150 hPa, so that the default pressure ranges of the boundary layer, lower troposphere, and upper troposphere were 1000 - 900 hPa, 900 hPa - 500 hPa, and 500 hPa - 150 hPa, respectively. The actual pressure differences of the layers were referred to as Δp_{BL}, Δp_{LT}, and Δp_{UT}. Deviations of a target grid cell from the target pressure difference were therefore

$$\delta p_{BL} = \Delta p_{BL} - \Delta p_{BL,tar} \tag{2}$$

$$\delta p_{LT} = \Delta p_{LT} - \Delta p_{LT,tar} \tag{3}$$

$$\delta p_{UT} = \Delta p_{UT} - \Delta p_{UT,tar}. \tag{4}$$

In general, convective mass fluxes tended to increase the pressure differences of grid cells from their target values. Conversely, horizontal mass fluxes, radiative subsidence, and dynamical vertical motions tended to relax the pressure differences of grid cells toward their target values. There was no background flow in the model.

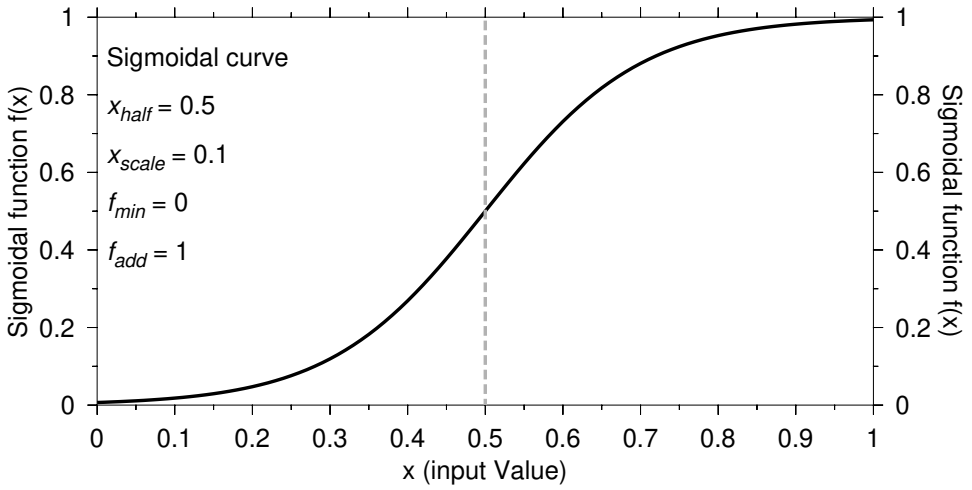

FIG. 4: The model uses sigmoidal functions to characterize the nonlinear dependence of several parameters on model variables. This plot shows a generic sigmoidal function $f(x)$ defined by four constants: the value f_{min} of $f(x)$ at low values of x, the value $f_{min} + f_{add}$ of $f(x)$ at large values of x, the value of x x_{half} where $f(x)$ changes most rapidly, and a parameter x_{scale} prescribing the steepness of $f(x)$ about x_{half}.

b. Sigmoidal parameterization

Deep convective rainfall is a strongly nonlinear function of the column relative humidity (or column water) (Holloway and Neelin 2009). We used sigmoidal functions to characterize this, and several other, nonlinear relationships in the model. These functions have the general form

$$f_{sig}(x) = f_{min} + \frac{f_{add}}{1 + e^{-x_{norm}}}. \tag{5}$$

Here, f_{min} is the value of the sigmoidal function at low values of x, while $f_{min} + f_{add}$ is the value of the function at large values of x. x_{norm} refers to the normalized value of x,

$$x_{norm} = \frac{x - x_{half}}{x_{scale}}. \tag{6}$$

x_{half} is the value of x where $f_{sig}(x)$ assumes a value half way between f_{min} and $f_{min} + f_{add}$, and is also the value of x for which $f_{sig}(x)$ changes most rapidly. The parameter x_{scale} determines the steepness of $f_{sig}(x)$ in the vicinity of x_{half}. Figure 4 shows a sigmoidal curve with particular choices for each of the four parameters.

c. Surface heat and moisture fluxes

The temperature and water vapor mass mixing ratio tendencies of the boundary layer due to heat and moisture fluxes from the ocean were defined as

$$dT_{BL}/dt = a_T(T_{SST} - T_{BL}) \tag{7}$$

$$dr_{v,BL}/dt = a_{r_v}(e_{s,SST} - e_{BL}). \tag{8}$$

T_{BL} and T_{SST} refer to the temperatures of the local boundary layer and sea surface temperature, $r_{v,BL}$ to the local boundary layer water mass vapor mixing ratio, $e_{s,SST}$ to the saturated vapor pressure of the local sea surface temperature, and e_{BL} to the water vapor pressure of the boundary layer. The parameters $a_T = 1 \times 10^{-10}\ s^{-1}$ and $a_{r_v} = 0.5 \times 10^{-6}\ Pas^{-1}$ were chosen to give reasonable values for the surface fluxes of sensible heat and water vapor.

d. Radiative subsidence

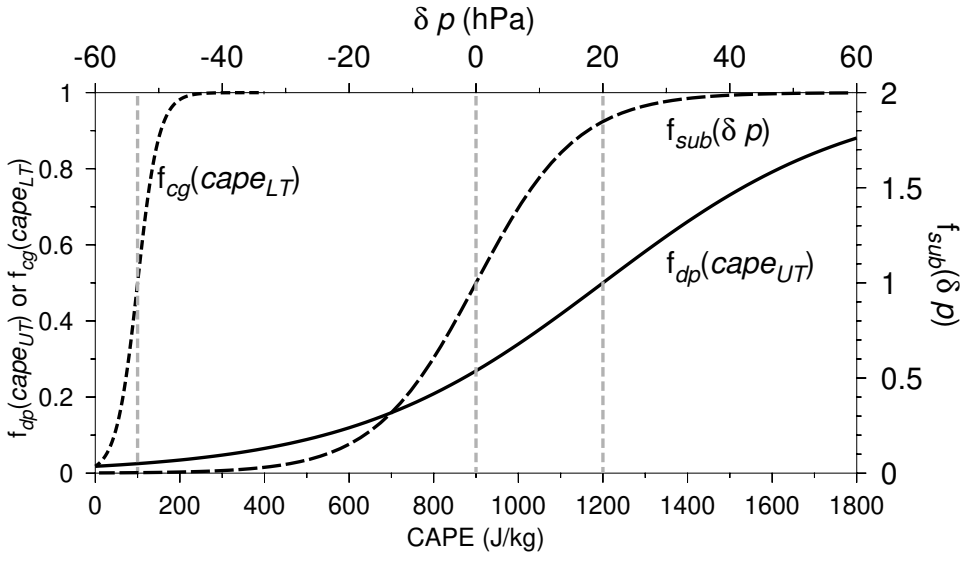

FIG. 5: Three of the sigmoidal function used in the model. $f_{cg}(cape_{LT})$ expresses the dependence of the congestus mass flux on lower tropospheric CAPE. $f_{dp}(cape_{UT})$ expresses the dependence of the deep convective mass flux on upper tropospheric CAPE. $f_{sub}(\delta p)$ characterizes the dependence of the radiative subsidence mass flux from the upper to lower troposphere on δp. This function modulates the subsidence mass flux between these two layers in such a way that the pressure thicknesses of grid cells do not deviate too strongly from their target values.

Radiative descent occurs from the upper troposphere to the lower troposphere, and from the lower troposphere to the boundary layer. It is based on a prescribed radiative cooling rate of $Q_{UT} = 0.8$

K/day in the upper troposphere, and Q_{LT} = 1.4 K/day in the lower troposphere. There is also a prescribed cooling rate of Q_{BL} = 1.5 K/day in the boundary layer, but this radiative cooling does not induce radiative descent. The radiative subsidence mass flux from the upper to lower troposphere was given by

$$m_{sub,UT} = f_{sub}(\delta p)\frac{Q_{UT}}{g c_{pd} \sigma_{UT,LT}}, \tag{9}$$

where g is the rate of gravitational acceleration due to gravity, c_{pd} is the specific heat of dry air at constant pressure, and $\sigma_{UT,LT}$ is the static stability between the upper and lower troposphere.

In order to keep the pressure thicknesses of the upper and lower troposphere reasonably close to their target values, the radiative subsidence was adjusted using the $f_{sub}(\delta p)$ function. This parameter is a sigmoidally increasing function of $\delta p = \delta p_{UT} - \delta p_{LT}$, and is parameterized using $\delta p_{min} = 0$, $\delta p_{scale} = 8$ hPa, $f_{sub,min} = 0$, and $f_{sub,add} = 2$. The dependence of $f_{sub}(\delta p)$ on δp with these parameters is shown in Figure 5. The upper tropospheric radiative subsidence is near zero when there is some combination of a large pressure deficit in the upper troposphere, or a large pressure surplus in the lower troposphere. Conversely, the radiative descent is twice as large when there is some combination of a large pressure surplus in the upper troposphere, or a large pressure deficit in the lower troposphere. The use of the $f_{sub}(\delta p)$ factor helped relax the pressure thicknesses of the upper and lower tropospheric grid cells toward their target values. Radiative descent from the lower troposphere to the boundary layer was defined in a similar manner, using the same $f_{sub}(\delta p)$ function, and the radiative cooling rate and static stability appropriate for the lower troposphere.

e. Length scales for horizontal transport of the two convective circulations

As discussed earlier, the radial variation of the temperature anomaly response to deep convection suggests that, near the equator, the majority of deep updraft subsidence extends a distance of roughly 1000 km, and stratiform downdraft uplift a distance of roughly 500 km, from strong convective events. Away from the equator, the length scale of each circulation would be expected to be inversely proportional to latitude. Therefore, for latitude values $lat(j)$ in excess of a particular $lat_{L,UT}$, with j referring to the meridional index of a grid cell, the upper tropospheric horizontal

transport length scale was defined as

$$L_{UT}(j) = L_{eq,UT}\frac{lat_{L,UT}}{lat(j)}. \qquad abs(lat(j)) > lat_{R,UT} \tag{10}$$

To avoid an infinity at the equator, the upper tropospheric length scale within $lat_{R,UT}$ of the equator was defined as

$$L_{UT}(j) = L_{eq,UT}[1 + 0.2(1 - lat_{norm}^2)], \qquad abs(lat(j)) < lat_{L,UT} \tag{11}$$

where $lat_{norm} = lat(j)/lat_{L,UT}$. Figure 3 shows the latitudinal variation of the upper tropospheric horizontal transport length scale about the equator using $lat_{L,UT} = 10^{\circ}$ and $L_{eq,UT} = 1100$ km. It would also be possible to assume that the upper tropospheric length scale was simply constant for latitudes within $lat_{L,UT}$ of the equator. However, this assumption is potentially undesirable because it would introduce a sudden change in the latitude variation of the horizontal transport length scale at this latitude.

In the model, the deep convective mass flux is roughly twice as large as the congestus mass flux. As a result, the majority of the horizontal flow in the boundary layer is induced by the deep circulation. The horizontal transport length scale of the boundary layer was therefore assumed to be the same as that of the upper troposphere. Horizontal flow in the lower troposphere is mainly a response to the vertical transport of mass from congestus clouds and downdrafts. We therefore adopted a parameterization of the lower tropospheric length scale in which $L_{eq,LT} = 500$ km and $lat_{L,LT} = 5^{\circ}$. The variation of the lower tropospheric length scale with latitude is also shown in Figure 3.

f. Horizontal transport

Horizontal motion in the model was highly simplified. Instead of adopting a set of dynamical equations, we assumed that the effect of the horizontal flow was to export mass from grid cells where there was a local pressure excess, and import mass toward grid cells where there was a local pressure deficit. The excess mass of a grid cell p was allocated to the surrounding (i, j) grid cells using a weight function. If grid cell (i, j) and grid cell p have the same latitude index j, they also have a common horizontal transport length scale $L_{UT}(j)$. If they are separated by a zonal distance

$D_p(i,j)$, we defined a normalized horizontal transport distance $D_{pn}(i,j) = D_p(i,j)/L_{UT}(j)$. The weight function between two points having the same j was then defined as a Gaussian function of this normalized distance.

$$W_p(UT,i,j) = exp[-D_{pn}^2(i,j)] \tag{12}$$

Because the horizontal transport length scales are a function of latitude, defining the weight function between two grid cells having the same longitude but different latitudes was more complicated. For two adjacent grid cells at the same longitude, we first determined their average horizontal transport length scale. We then calculated the normalized distance between them, and used Eq. (12) to determine their weight function. For two grid cells differing by more than one grid cell in the meridional direction, the weight function was defined as the product of all intermediary weight functions of adjacent grid cells. Finally, for two grid cells having differing longitude and latitude, the weight function between them was defined as the product of the weight function along the zonal direction with the weight function along the meridional direction. Figure 6 shows the spatial variation of an upper and a lower tropospheric weight function with respect to their indicated start points p. The decrease in the circulation length scales with distance from the equator implies that the majority of the horizontal transport in the model occurs between 15 ^{o}S and 15 ^{o}N.

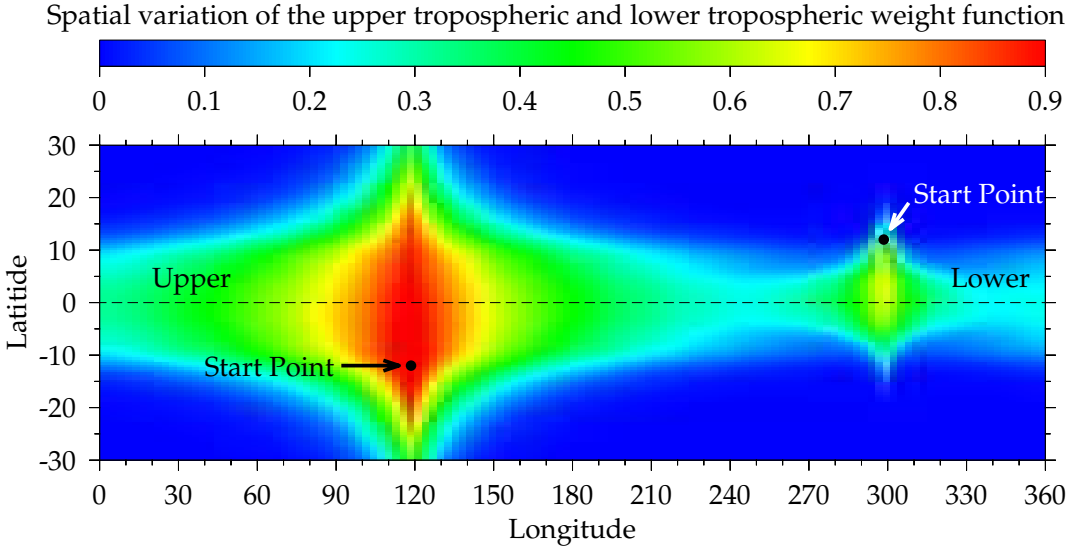

FIG. 6: Spatial variation of the upper and lower tropospheric weight functions. The weight functions define the spatial region over which horizontal transport occurs from a given starting point. The starting point for the upper tropospheric weight function was at 12 ^{o}S. For the lower tropospheric weight function, the starting point was at 12 ^{o}N. The length scale for horizontal transport increases toward the equator. This implies that the majority of horizontal transport toward, or away from, a grid point will be on the equatorial side of the starting point.

Because of the earth's rotation, it is not required that the weight functions be symmetric in the zonal direction. Therefore, we allowed the effective horizontal transport length scale in the eastward direction to be slightly larger or smaller than the horizontal transport length scale in the westward direction. Going in an eastward direction from the original grid point, the length scale was multiplied by a zonal asymmetry factor $f_{L,asym}$. Going westward from the original grid point, the length scale was divided by this asymmetry factor.

$$L_{UT,east}(j) = f_{L,asym} L_{UT}(j) \tag{13}$$

$$L_{UT,west}(j) = L_{UT}(j) / f_{L,asym} \tag{14}$$

In practice, the rainfall variance of the model was extremely sensitive to small deviations of the zonal asymmetry factor from one. We therefore only discuss simulations in which either $f_{L,asym} = 1$ (no zonal asymmetry) or $f_{L,asym} = 0.95$ (slightly larger horizontal transport length scale in the westward direction).

To determine whether the grid cell at point p should export mass to, or import mass from, its surrounding grid cells, we first defined the sum of all weight functions about point p.

$$W_p(UT, sum) = \sum_{i,j} W_p(UT, i, j) \tag{15}$$

The local mean pressure thickness in the neighborhood of grid cell p was then defined as,

$$\overline{\Delta p_{UT,p}} = \frac{\sum_{i,j} W_p(UT, i, j) \Delta p_{UT,i,j}}{W_p(UT, sum)} \tag{16}$$

If the pressure thickness at point p deviated from this locally weighted value, the amount of mass exported from or imported toward point p was given by,

$$\delta m_p = f_{move}(\Delta p_{UT,p} - \overline{\Delta p_{UT,p}})/g, \tag{17}$$

where positive δm_p implies an export of mass, and negative δm_p the reverse. The parameter f_{move} determines the rapidity with which horizontal transport reduced anomalies in the local pressure thickness of a grid cell. For grid cells at the equator, $f_{move,eq} = 0.6$. For grid cells off the equator,

this value was multiplied by the ratio of the integrated weight function about that point, relative to the value at the equator.

$$f_{move} = \frac{W_p(UT, sum)}{W_{eq}(UT, sum)} f_{move,eq} \tag{18}$$

Horizontal transport on the lower tropospheric and boundary layers was handled in an identical fashion, except for the use of a different transport length scale in the lower troposphere.

g. Vertical dynamics

Horizontal transport generates net convergent inflow toward some grid cells, and net divergent outflow from other grid cells. The mass convergence m_{conv} at grid cell was defined as the net mass per unit area added to a grid cell in one time step by horizontal transport. Upward vertical motion in the lower troposphere was assumed to be linearly proportional to the mass convergence of the lower level, minus the mass convergence of the upper level.

$$m_{dyn,LT} = f_{dyn}(m_{conv,BL} - m_{conv,LT}) \tag{19}$$

The dimensionless parameter $f_{dyn} = 0.24$ determines the response time of vertical transport to a differential rate of horizontal mass convergence between two levels. A similar equation was used to define the dynamical vertical motion between the lower and upper troposphere. With this parameterization, upward motion between levels was forced by some combination of convergence at the lower level and divergence at the upper level, and downward motion by the reverse combination. The effect of dynamical vertical motion between two levels was therefore to dampen changes in the relative mass of two levels caused by the horizontal flow.

h. Congestus convection

Congestus clouds transport mass from the boundary layer to the lower troposphere. The congestus mass flux m_{cg} was assumed to be an increasing function of the CAPE between the boundary layer and the lower troposphere ($cape_{LT}$) and the column relative humidity ($colrh$), and in phase with the total (dynamic and radiative) vertical motion in the lower troposphere.

$$m_{cg} = a_{cg} f_{cg}(cape_{LT}) f_{cg}(colrh)(m_{dyn,LT} + m_{sub,LT}) \tag{20}$$

The parameter $a_{cg} = 3$ controls the amplitude of the congestus response to upward motion in the lower troposphere. The sigmoidal functions $f_{cg}(cape_{LT})$ and $f_{cg}(colrh)$ were used to modulate the congestus response based on available lower tropospheric CAPE and column relative humidity, and are shown in Figures 5 and 7, respectively. Congestus clouds were assumed to respond effectively instantaneously to the net dynamical forcing $m_{dyn,LT} + m_{sub,LT}$ (positive upward). The congestus mass flux was set to zero when the net vertical motion was downward.

Some of the rainfall that is generated by congestus clouds evaporates into the lower troposphere. The evaporated congestus rainfall fraction $f_{evap,cg}$ is a sigmoidal function of the relative humidity of the lower troposphere. It decreases from $f_{evap,cg} = 0.5$ at low relative humidity to $f_{evap,cg} = 0.0$ at high relative humidity. In addition, evaporation of congestus rainfall is not permitted to result in a lower tropospheric relative humidity in excess of $rh_{evap,add} = 0.80$.

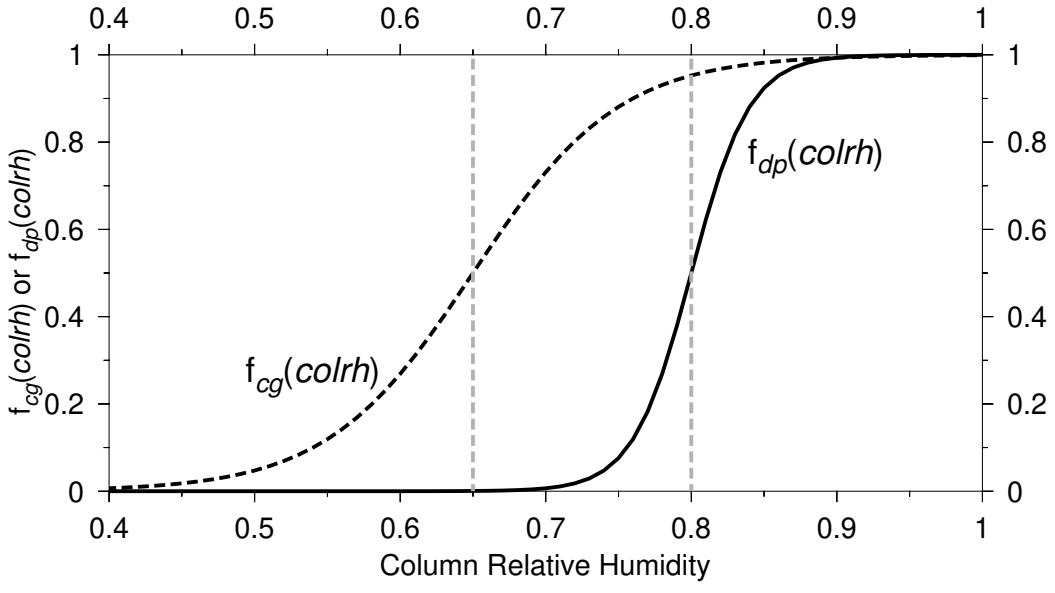

FIG. 7: Observations indicate that the congestus and deep convective mass fluxes have a nonlinear dependence on the column relative humidity. This is characterized in the model using sigmoidal functions. The nonlinear threshold column relative humidity for congestus mass was assumed to be lower, and the rate of increase more gradual, than for deep convective clouds.

i. Deep convection

The deep convective mass flux was defined using a method very similar to the congestus mass flux. However, rather than responding instantaneously to the net vertical mass flux in the lower troposphere, we assumed that the deep convective mass flux tendency was in phase with the net vertical motion of the lower troposphere. Therefore, at each time step, the initial deep convective

mass flux $m_{dp,i}$ was retained from the previous time step, and then adjusted by an increment proportional to $(m_{dyn,LT} + m_{sub,LT})$. For net upward motion in the lower troposphere, we assumed

$$m_{dp} = m_{dp,i} + a_{dp,+} f_{dp}(cape_{UT}) f_{dp}(colrh)(m_{dyn,LT} + m_{sub,LT}). \quad (21)$$

For net downward motion in the lower troposphere, we assumed

$$m_{dp} = m_{dp,i} + a_{dp,-}[1. - f_{dp}(cape_{UT}) f_{dp}(colrh)](m_{dyn,LT} + m_{sub,LT}). \quad (22)$$

We used $a_{dp,+} = 6$ for upward lower tropospheric motion, and $a_{dp,-} = 10$ for downward lower tropospheric motion. The functions $f_{dp}(cape_{UT})$ and $f_{dp}(colrh)$ were used to modify the change in m_{dp} to vertical motion depending on the local value of upper tropospheric CAPE and the column relative humidity. These were again parameterized using sigmoidal functions and shown in Figures 5 and 7. Rainfall from deep convective clouds was also allowed to evaporate in the lower troposphere, with the parameterization being identical to that used for cumulus convection.

Downdrafts were generated by the evaporation of deep convective rainfall, and transported mass from the lower troposphere to the boundary layer. The maximum downdraft mass flux was a prescribed fraction f_{dn} of the deep updraft mass flux. This fraction increased from $f_{dn} = 0$ at low values of deep mass flux, to $f_{dn} = 0.8$ at large values of deep updraft mass flux. The evaporation of deep rainfall used in generating this downdraft mass flux was assumed to be the minimum required to generate a negative downdraft buoyancy of $b_{dn} = -0.01$ m/s^2 in the boundary layer, with the total deep rainfall evaporation fraction not allowed to exceed 0.6. The downdraft mass flux was set to zero if the lower tropospheric relative humidity was larger than $rh_{dn,add} = 0.85$.

j. Drizzle and anvil rain

The relative humidity of the boundary layer and the upper troposphere layers had a tendency to exceed realistic values. We prescribed a maximum boundary layer relative humidity $rh_{BL,max} = 0.85$, and a maximum upper tropospheric relative humidity $rh_{UT,max} = 0.90$. The excess moisture at grid cells that exceeded these limits was converted to drizzle rain and anvil rain respectively. This rainfall production was done in a way which conserved moist enthalpy, and therefore resulted in an increase in the temperature of the boundary layer or upper troposphere.

5. Results

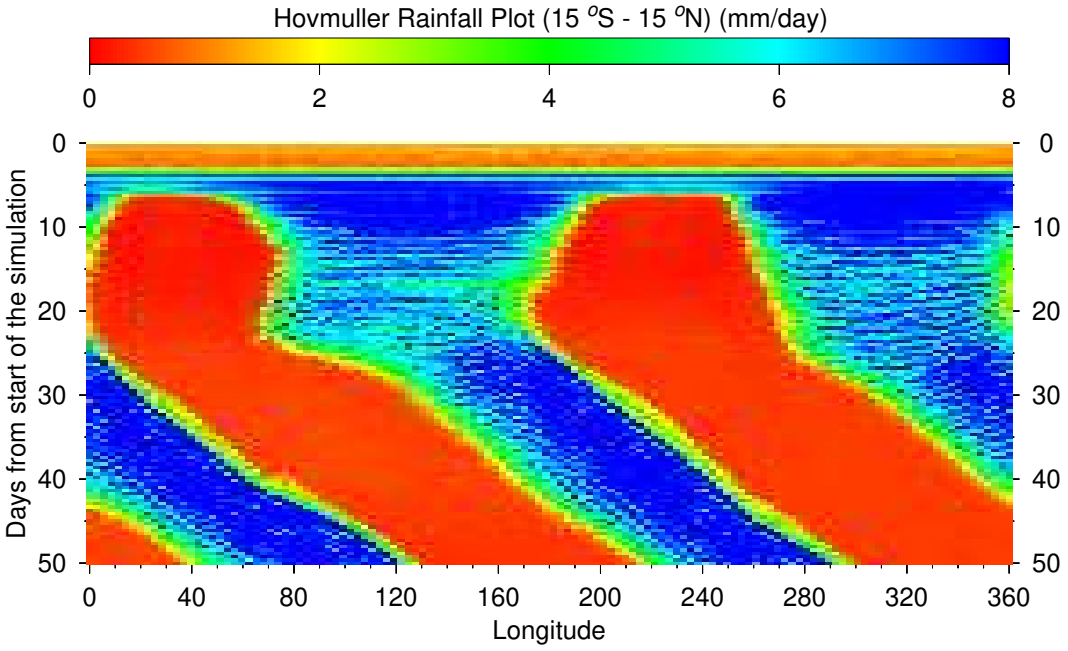

FIG. 8: Hovmöller diagram of the latitudinally averaged (15 °S - 15 °N) total rainfall for the first 50 days of the default version of the model. There is a rapid increase in rainfall rate near day 3, when the column relative humidity becomes sufficiently large to support convection. The rainfall is initially zonally uniform. Large scale clusters of enhanced rainfall appear at day 5. These clusters are initially stationary, but begin to propagate eastward at day 25.

a. Hovmöller rainfall diagram

Figure 8 shows a Hovmöller diagram, in which the total rainfall rate of the model was averaged between 15 °S and 15 °N. The zonal asymmetry parameter was assigned a value $f_{L,asym} = 0.95$. In this case, the induced horizontal mass flux in response to a local mass surplus or deficit was slightly larger in the western direction. There is an initial adjustment period of several days in which the rainfall rate is near zero. This occurs because the initial relative humidity of the model is too low to support convection. When rainfall first develops, it is zonally uniform. At day 5, rainfall becomes concentrated into two longitude bands of roughly 90^{o} in width. Although these bands are initially stationary, they start to propagate eastward at day 25 with a speed of $v = 6.43$ m/s.

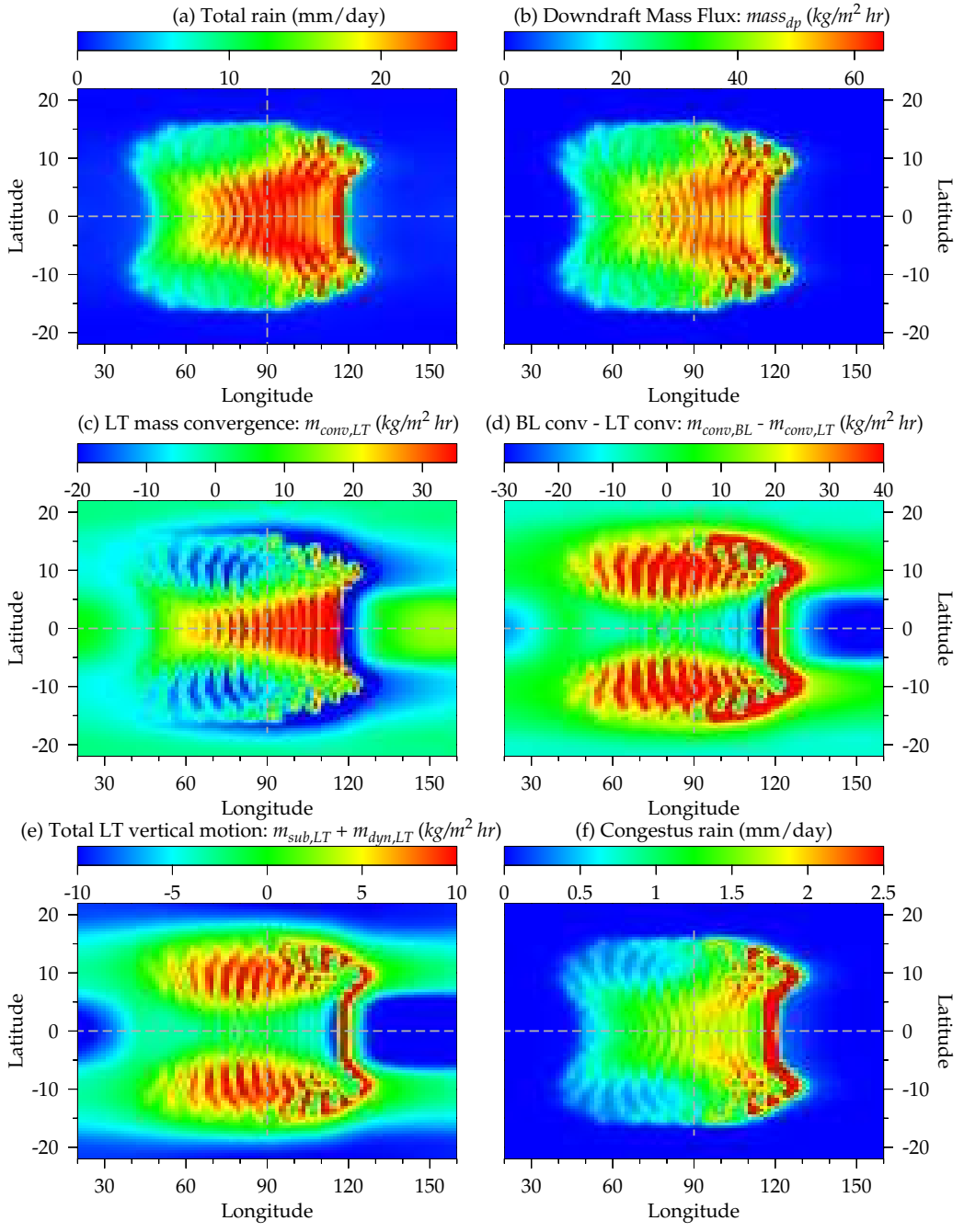

FIG. 9: Mean horizontal structure of the MJO events simulated by the model. The composites have been constructed by identifying, after a 25 day spinup, an MJO center at every time step of a 300 day model run. Model variables are then averaged about that location. Each MJO center is mapped to 90 ^{o}longitude at the equator. (a) Total rain, (b) Downdraft mass flux, (c) Lower troposphere mass convergence. The lower tropospheric mass required by the downdraft circulation within the MJO is preferentially extracted from grid cells in front of the MJO. (d) Boundary layer convergence minus the lower tropospheric divergence. This convergence difference is proportional to the lower tropospheric dynamical vertical mass flux. (e) The total (subsidence + dynamical) vertical mass flux of the lower troposphere. (f) Congestus rainfall. This is similar to the total lower troposphere vertical mass flux shown in (e), but is modulated by the lower tropospheric CAPE and column relative humidity, which tend to be larger within the MJO.

b. Mean MJO horizontal structure

Figure 9 shows some aspects of the mean horizontal structure of the MJO events simulated by the model. The composite was constructed as follows. After a spinup period of 25 days, we identified the grid cell along the equator at each time step, between 90 E and 180 E, which had the largest rain rate, when averaged over all grid cells in the model within 90^o to either side of the grid cell. This grid cell was assumed to be the center of a simulated MJO. We then constructed a composite MJO pattern by averaging model variables about this grid cell. The model simulations were run for 300 days.

The upper left panel of Figure 9 shows the total rain rate, i.e. the sum of all types of rain generated by the model, minus all types of evaporation. The rain rate is larger along the eastern side of the MJO in the direction of propagation, and larger closer to the equator. Rainfall is also organized into squalls lines oriented along the meridional direction. The upper right panel of Figure 9 shows the downdraft mass flux. Most of the rainfall in the model originates from deep convection, so that the downdraft mass flux pattern is very similar to the total rain pattern. Downdrafts remove mass from grid cells in the lower troposphere and transport this mass to the boundary layer. Lower tropospheric grid cells where there is a large downdraft mass flux will therefore typically have a mass deficit. This mass deficit generates an inward horizontal mass flux from the surrounding atmosphere, extending over a spatial scale equal to the local lower tropospheric length scale for horizontal transport. The middle left panel of Figure 9 shows the convergence in the lower troposphere due to this horizontal mass flux. There is a region of strong convergence along the equator where there is a large inward horizontal mass flux toward grid cells with the largest downdraft mass flux. The nearby regions shown in blue indicate the divergent regions which supply the mass required to sustain the downdraft mass flux. The middle right panel of Figure 9 shows the convergence of the boundary layer, minus the convergence of the lower troposphere. As shown in Eq. (19), upward dynamical motion between two layers occurs in the model when there is some combination of mass convergence in the lower level and mass divergence in the lower level. The regions shown in red in Figure 9(d) can therefore be taken to roughly indicate the regions within an MJO where the upward branch of the downdraft congestus circulation is strongest. This circulation generates upward motion within two symmetric lobes each between roughly 5^o and 15^o to either side of the equator, as well as along the forward leading

edge of MJO. In the model, the congestus mass flux is in phase with the total lower tropospheric vertical mass flux, which is the sum of the dynamical and radiative mass flux, $m_{dyn,LT} + m_{sub,LT}$. This quantity is shown in the lower left panel of Figure 9. It is quite similar to the pattern shown in Figure 9(d), indicating that within an MJO, the lower tropospheric vertical mass flux is dominated by the dynamical component. The bottom right panel of Figure 9 shows the congestus rainfall generated by the model. The congestus rainfall rate is strongest at the eastward leading edge of MJO, consistent with previous suggestions (Kiladis et al. 2005; Chen and Wang 2020). Figure 9(e) shows that the dynamical forcing for congestus cloud formation is also very strong within the two lobes in the middle and to the rear of the MJO. However, $cape_{LT}$ is reduced within these two lobes, so that the sigmoidal function $f_{cg}(cape_{LT})$ in Eq. (20) is too small to support congestus development, despite the strength of the dynamical forcing.

c. Mean longitudinal surface pressure variation

Figure 10(a) shows the mass convergence of the composite MJO pattern, averaged between 5^{o}S and 5^{o}N for each of the three model levels, and plotted as a function of longitude. The irregularity of the mass convergence curves is due to the internal squall line structure of the MJO. The upper tropospheric mass divergence, shown here as a negative convergence, is roughly twice as large as the boundary layer and lower tropospheric mass convergence. The downdraft mass flux is therefore roughly one half as large as the deep updraft mass flux. The surface pressure tendency can be calculated from the residual of the three mass convergence terms. The lower plot of Figure 10 shows this residual in units of hPa/day. As would be expected, this tendency is negative in the leading eastern half of the MJO, and positive in the rearward western half of the MJO. The black curve shows the surface pressure anomaly, defined in the model as a deviation from 1000 hPa. Due to deep convective detrainment, upper tropospheric grid cells within the MJO have a mass surplus. This mass surplus generates a large scale upper tropospheric horizontal mass export. In the leading eastern half of the MJO, this mass export is larger than the inward transport of mass occurring on the BL and LT levels, generating a net negative surface pressure tendency. In the rearward western half of the MJO, the situation is reversed, with the surface pressure tendency becoming positive, and generating a positive surface pressure anomaly to the rear of the MJO.

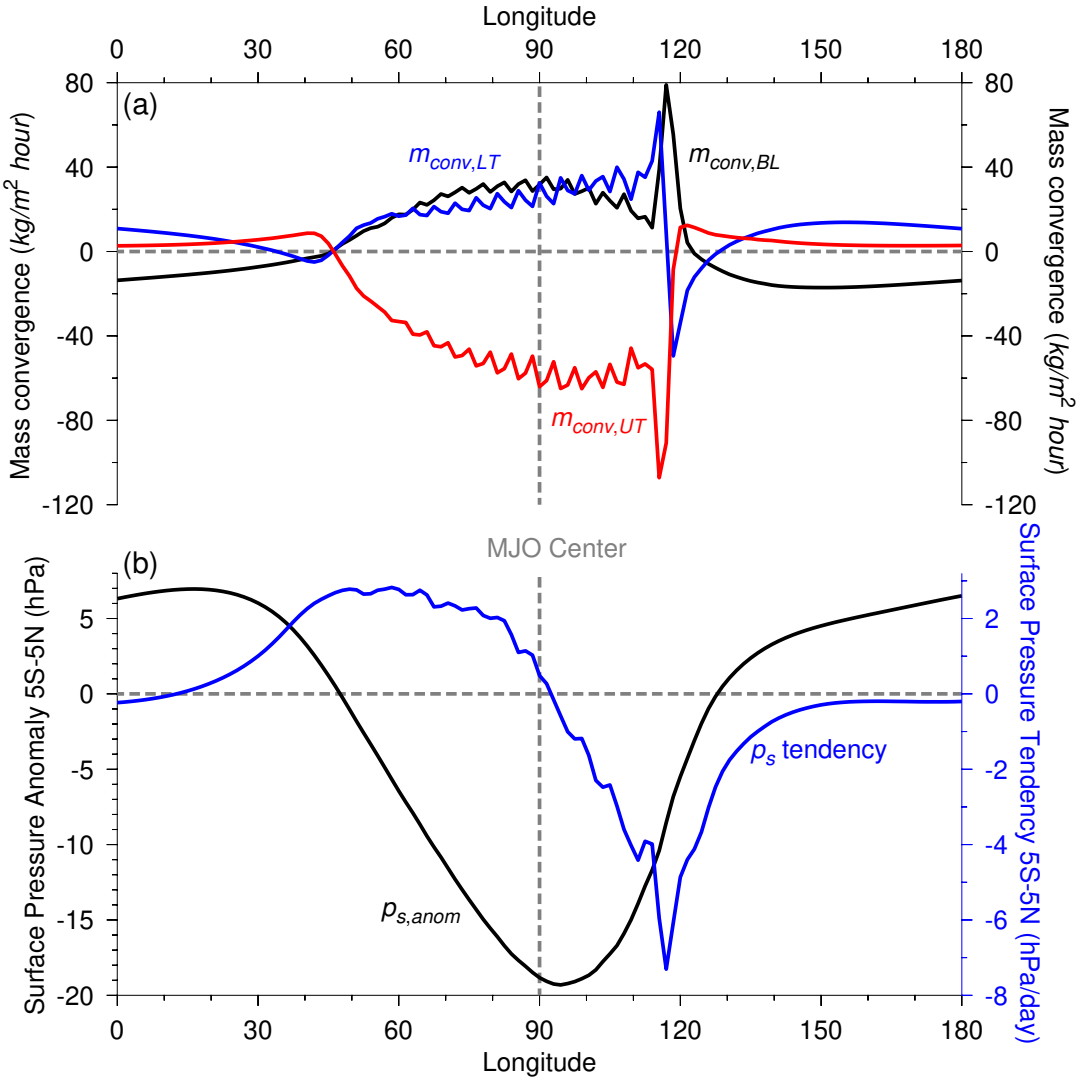

FIG. 10: (a) Longitudinal variation along the equator (5 ^{o}S - 5 ^{o}N) of the mass convergence of each layer due to horizontal transport, obtained from the MJO composite pattern. Within the simulated MJO events, the upper tropospheric divergence is roughly twice as large as the convergence of the other two layers. (b) The curve shown in blue is the surface pressure tendency (in a frame of reference moving with the MJO) arising from a non-zero residual of the three mass convergence terms shown in (a). The negative surface pressure tendency in the leading half of the MJO generates the large negative surface pressure anomaly at the center of the MJO, shown in black.

The left panel of Figure 11 shows the composite MJO surface pressure anomaly pattern. There is a strong negative surface pressure anomaly to the east of the MJO center. Although the model does not have explicit horizontal winds, winds in the boundary layer can be calculated from the assumptions that the wind field is steady, that there is a three way force balance between the pressure gradient, Coriolis, and frictional accelerations, and that the radius of curvature of the wind field is sufficient large that the centripetal acceleration can be ignored. The amplitude of the zonal wind

field shown on the right of Figure 11 was calculated using an acceleration due to friction equal to $-\epsilon\mathbf{V}$, with $\mathbf{V}$ the wind vector and the friction coefficient $\epsilon = 5 \times 10^{-5} s^{-1}$. As would be expected, the zonal pressure gradient pattern is associated with westerly winds to the rear of the MJO and easterly winds at the leading edge of the MJO. In the model, the relative strength of the easterly and westerly winds is affected by the zonal asymmetry parameter $f_{L,asym}$, with stronger westerly winds developing when the zonal asymmetry parameter is smaller (i.e. increased horizontal import of boundary layer mass into the MJO from the west).

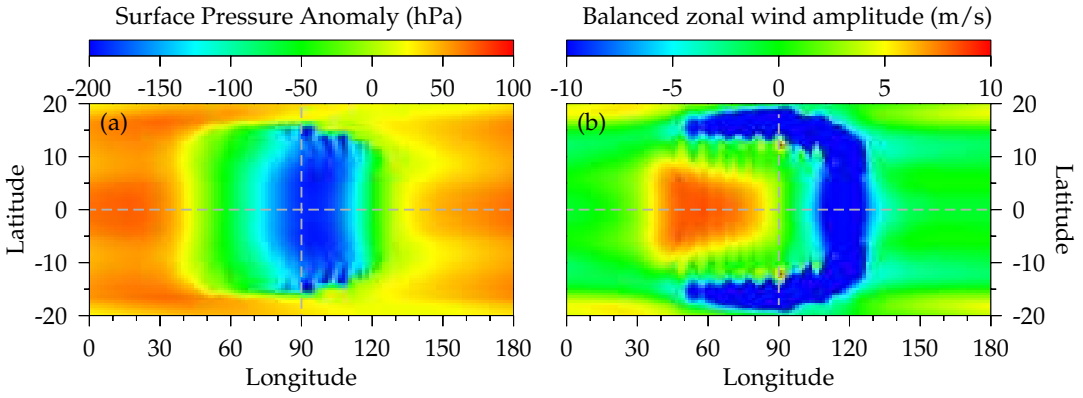

FIG. 11: (a) Spatial variation of the surface pressure anomaly about the MJO composite. There is a negative pressure anomaly in the leading half of the MJO. (b) Amplitude of the zonal wind in the boundary layer, assuming a three way balance between the zonal pressure gradient, Coriolis, and frictional accelerations. There is a strong westerly inflow at the rear of the composite MJO.

d. Mass divergence about high rain events

It is difficult to directly measure clear sky vertical mass fluxes in the atmosphere. However, mass divergence profiles about strong convective events provide some insight into the relationship between vertical motion and convective mass fluxes in the tropics (Mapes and Houze 1995). The mass divergence profiles shown in Figure 12 were generated by combining wind data from rawinsonde arrays in Borneo and the Malay Peninsula (Mitovski et al. 2010). The spatial scale of each array ($\sim$ 250 km) is smaller than the length scale of the downdraft congestus circulation. At any given time, the divergence profile of an array should therefore reflect the preferred cloud type during that particular phase of the downdraft circulation.

Rain events were considered to occur at times between 1998 and 2008 in which the mean TRMM rain rate within each array was in the top 5 % for that month. The mean TRMM rain rate profile within the two arrays is shown in Figure 13. Simultaneous wind profiles from an array that

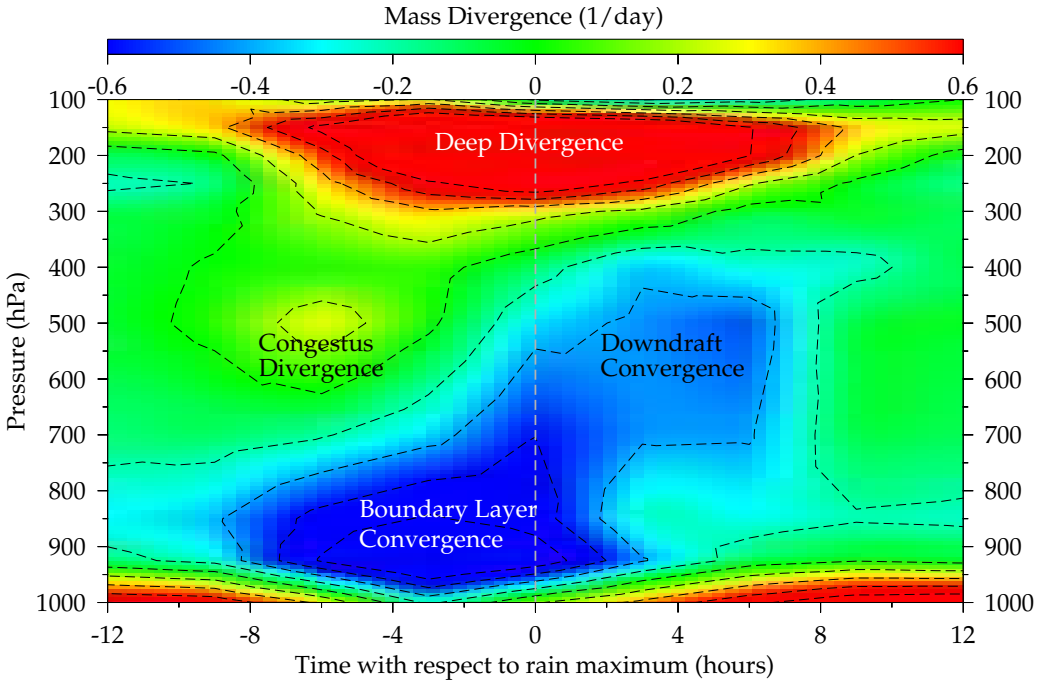

FIG. 12: Composite mass divergence pattern during the growth and decay of high rain events. It was obtained by combining horizontal wind profiles from triangular rawinsonde arrays in Borneo and the Malay Peninsula between 1998 and 2008 (Mitovski et al. 2010). The mean temporal variation of the TRMM rain rate within the two arrays is shown in Figure 13. The mid-level mass divergence dipole is consistent with the tilted ω structures that usually characterize convective development (Inoue et al. 2020).

occurred within 24 hours of the TRMM rain event times were then used to construct a composite diagram of the mean vertical variation of mass divergence during the growth and decay of high rain events. The peak in boundary layer convergence occurs roughly 3 hours prior to peak rainfall, while the peak in upper tropospheric divergence occurs 1-2 hours after peak rainfall. Although these divergence features have a maximum amplitude of ~ 1.4 day^{-1}, we have used a smaller scale in Figure 12 to emphasize the mid-level divergence features. Of particular interest is the mid-level divergence dipole, consisting of a 500 hPa divergence peak 6 hours prior to peak rainfall, and a broader convergence peak centered 4 hours after peak rainfall.

The mass divergence pattern shown in Figure 12 was used an observational target to guide the development of the convective parameterization used in the model. We considered rain events to occur when the total rain rate at any time step exceeded 25 mm/day. Most of these rain events occur within the meridional squall lines shown in Figure 9(a). We then used the convergent mass fluxes at the three levels, generated by the horizontal flow, normalized by the mass of each grid cell, to generate the divergence pattern shown in upper panel of Figure 13. The simulated divergence pattern is broadly similar to the observed pattern shown earlier in Figure 12, and in particular,

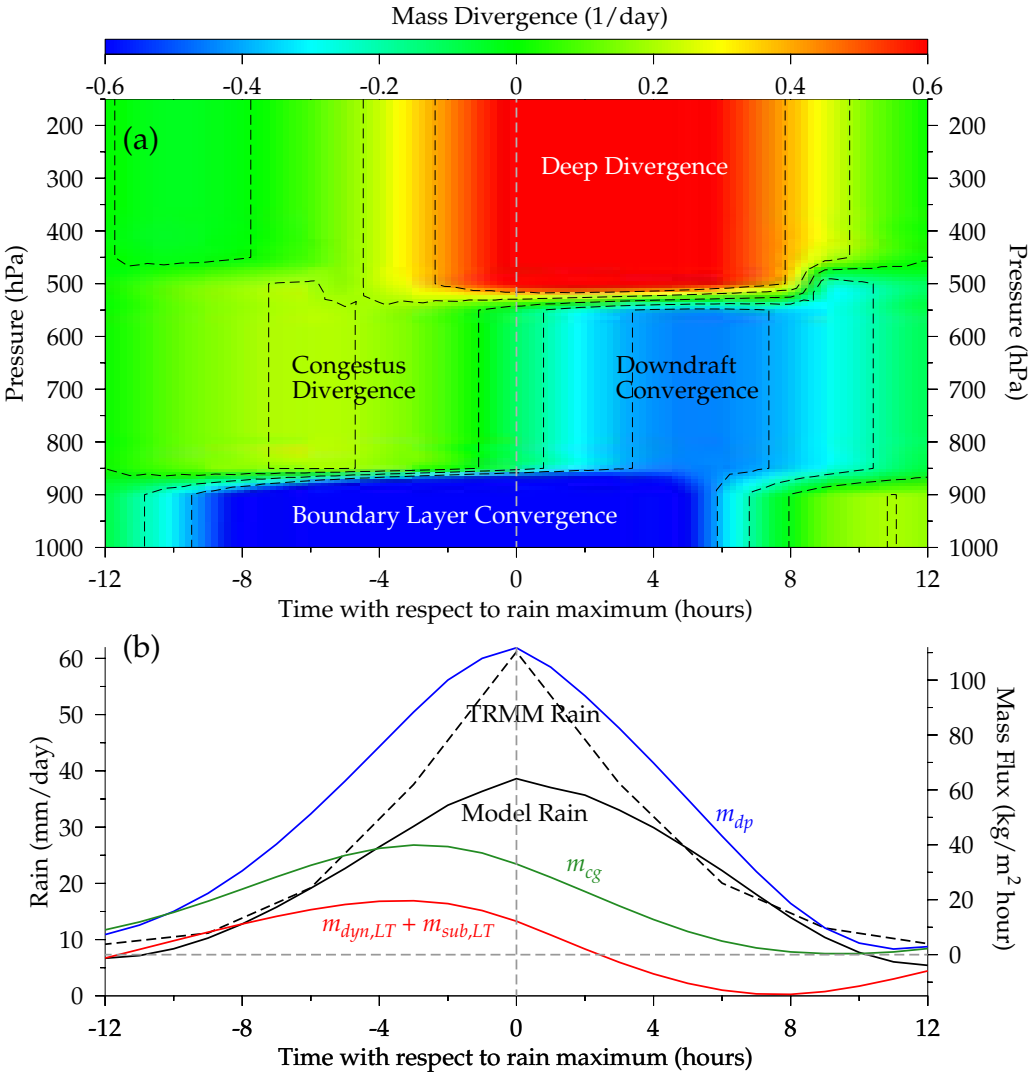

FIG. 13: (a) The top panel shows the variation in mass divergence during the growth and decay of simulated rain events, obtained from the three model levels. (b) The dashed black curve shows the mean TRMM rain rate variation within the two rawinsonde arrays used to construct the observed mass divergence pattern shown in Figure 12. The solid black curve shows the mean rain rate variation during the rain events of the model. The blue and green curves show the variation in the deep and congestus convective mass fluxes, respectively. The congestus mass flux, and the deep mass flux tendency, are proportional to the total (subsidence + dynamical) lower tropospheric vertical motion, shown in red.

appears to be in better agreement with observations than some larger scale models (Mitovski et al. 2010, 2012). The deep divergence of the model is somewhat lagged relative to the observations, and because of the limited vertical resolution of the model, the simulated mid-level congestus divergence peak is elongated in the vertical relative to the observed congestus peak.

The lower plot of Figure 13 shows the temporal variation of simulated total rainfall during the growth and decay of high rain events, together with the TRMM rain rate averaged over the two

rawinsonde arrays. Although the two curves are similar, the TRMM rain rate is more sharply peaked at $t = 0$, reflecting the reduced rainfall variance of the model with respect to TRMM. This plot also shows the deep mass flux m_{dp}, the congestus mass flux m_{cg}, and the sum of the dynamic and subsidence lower tropospheric mass flux $m_{dyn,LT} + m_{sub,LT}$. By construction, the congestus mass flux and the deep mass flux growth rate are in phase with the total upward lower tropospheric mass flux.

In the model, congestus detrainment generates positive mass anomalies in lower tropospheric grid cells. The parameterization for horizontal transport then exports this excess mass over a spatial scale equal to the local length scale of the downdraft circulation. This mass export generates the mid-level divergence feature prior to peak rainfall in the model. This simulated congestus divergence maximum occurs several hours prior to the peak in congestus mass flux because the downdraft mass flux (not shown) is in phase with the deep mass flux. Downdrafts remove mass from the lower tropospheric layer, and therefore progressively erode the positive lower tropospheric mass anomaly generated by congestus detrainment, as peak rain is approached. After peak rain, the downdraft mass flux is significantly larger than the congestus mass flux, and generates a progressively larger negative mass anomaly in the lower troposphere. This negative mass anomaly drives horizontal inflow from the surrounding atmosphere, which gives rise to the mid-level downdraft convergence feature after peak rainfall shown in Figure 13. The downdraft convergence feature then progressively weakens as the rain rate decays, the downdraft mass flux also dissipates, and the negative lower tropospheric mass anomaly generated by the downdrafts is eroded by inflow from the horizontal circulation.

e. Rain power spectrum

Wheeler Kiladis diagrams (Wheeler and Kiladis 1999) are widely used to assess the accuracy with which climate models simulate organized forms of tropical rainfall variance. Tropical rainfall is first expressed as a sum of symmetric and antisymmetric components about the equator. Each component is then averaged within some latitude band centered at the equator (here 16 ^{o}S - 16 ^{o}N). Each of the two rainfall components is a function of longitude and time. This time series is then expressed as a power spectrum in terms of a longitudinal wavenumber k and frequency ν. In most cases, the symmetric and antisymmetric power spectra are normalized by a smoothed background

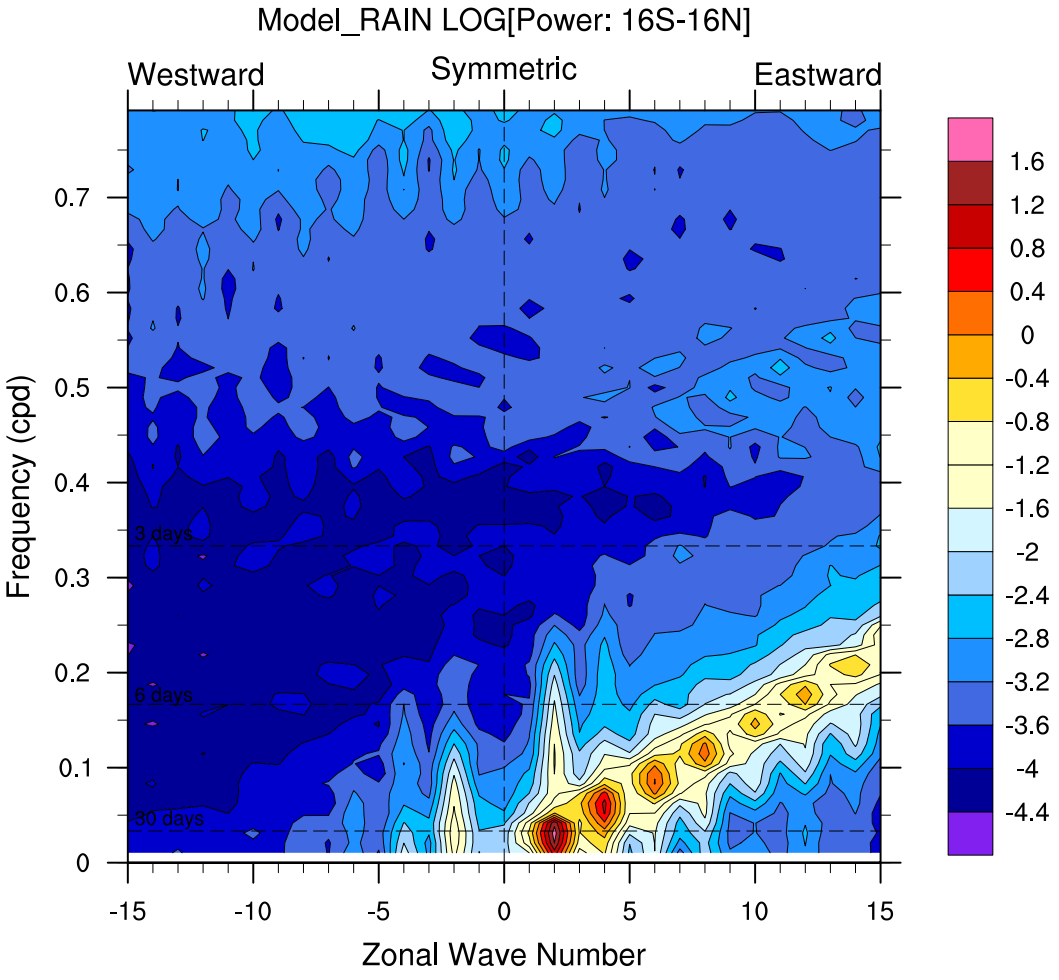

FIG. 14: Zonal wavenumber-frequency symmetric power spectra from the model using 300 days (minus 25 day spinup) of 16 ^{o}S - 16 ^{o}N total rainfall. Simulated MJO variance is largest for zonal wavenumber 2, but there are weaker harmonics at zonal wavenumbers 4, 6, 8, 10, etc, distributed along a linear dispersion curve.

spectrum to emphasize regions of enhanced power. Here, however, there was sufficient power in the simulated raw MJO spectral peak that this was unnecessary.

Figure 14 shows the logarithm of the power of the raw symmetric spectrum of a 300 day run of the model, after a 25 day spinup. For comparison, Figure 15 shows the logarithm of the power of the raw symmetric spectrum obtained from five years of TRMM rainfall (2003 - 2007). Both plots were produced using the wkSpaceTime routine of the NCAR Command Language (NCL). The two spectra have different scales, with the power spectrum of the model extending over a much larger

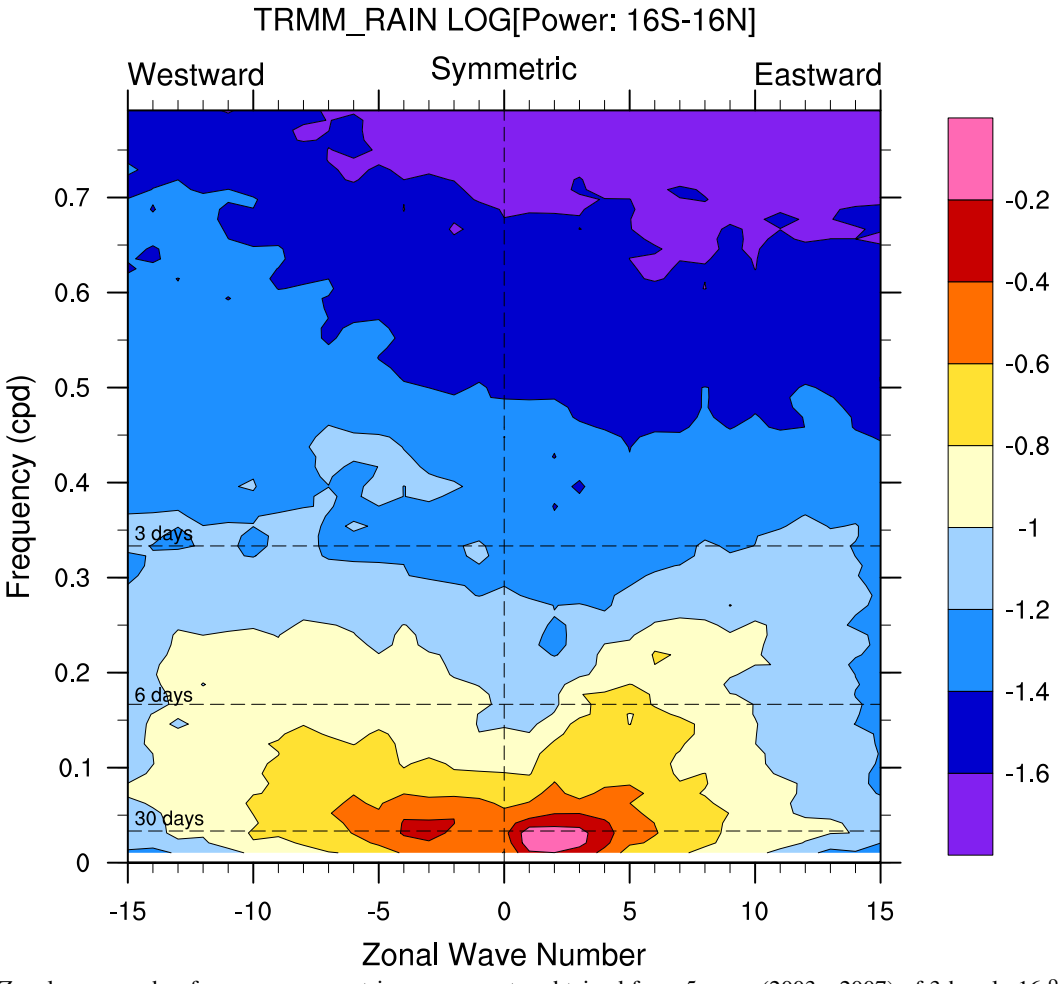

FIG. 15: Zonal wavenumber-frequency symmetric power spectra obtained from 5 years (2003 - 2007) of 3 hourly 16 ^{o}S - 16 ^{o}N TRMM 3B42 rainfall data. Enhanced MJO variance occurs between zonal wavenumbers 1 and 4.

range of amplitudes. In the TRMM spectrum, the MJO related rainfall variance is associated with a peak in the eastward propagating power with frequencies less than 0.05 cpd (i.e. periods longer than 20 days), and a range of global wave numbers from 1 to 5. The model spectrum exhibits a peak slightly below the dashed line showing the 30 day period, centered at global wave number 2.

At any given time, the variation in 16 ^{o}S - 16 ^{o}N rainfall with longitude is not purely sinusoidal, so that higher order harmonics at all even values of zonal wave number are also present. The dispersion curve is clearly linear, with a slope corresponding to a phase speed of 6.80 m/s (inferred from the dispersion curve intersecting the zonal wave number 15 axis with a frequency of 0.22).

Therefore, although the dominant frequency and wavenumber of the simulated MJO are similar to that of the TRMM dataset, the peak in spectral space of the modeled MJO is much more sharply defined, and is part of a linear dispersion curve extending to successively weaker higher order harmonics, whose slope is roughly equal to the observed MJO propagation speed.

f. MJO propagation speed

The propagation speed of the MJO in the model can be inferred from the movement of the MJO center. In the 300 day default simulation of the model, the MJO has a speed of 6.43 m/s to the east. Observed MJO's have a finite lifetime, are strongly damped (Lin et al. 2005), and occur in a variety of SST, moisture, and background flow configurations. They are therefore usually characterized as having a range of propagation speeds of 2 - 8 m/s (Chen and Wang 2020).

One unrealistic aspect of the model is that the horizontal motions generated by convective entrainment and detrainment occur instantaneously, as opposed to being generated by outwardly propagating waves with a finite phase speed. The vertical motions of the background atmosphere therefore respond very quickly to the mass anomalies generated by convective mass transport. The propagation speed of the MJO events simulated by the model is therefore constrained mainly by lags in the convective response to vertical motion.

The top panel of Figure 16 shows the mean longitudinal variation of the deep convective mass flux m_{dp}, and the net deep convective mass flux tendency $m_{dp,prod}$, at the eastern leading edge of the mean MJO pattern. The leading edge is defined as the grid cell where m_{dp} assumes its largest value. The oscillation in the net m_{dp} tendency, shown in blue, generates the squall line multiscale structure of the MJO. The forward advance of the MJO is limited by the timescale with which m_{dp} can respond to the m_{dp} tendency. In this case, the value of the deep convective mass flux at the leading edge of the MJO ($m_{dp,LE}$) should equal the cumulative amount of deep convective mass flux production at the leading edge (LE) grid cell over the previous several days. Several days would be sufficient because both m_{dp} and $m_{dp,prod}$ relax to zero sufficiently in advance of the MJO envelope.

$$m_{dp,LE} = \int_{days}^{previous} m_{dp,prod} dt \tag{23}$$

If we assume that the shape of the deep convective mass flux tendency is fixed relative to the leading edge of the MJO, and the MJO propagation speed is defined as v_{MJO}, we can let $dt = dx/v_{MJO}$,

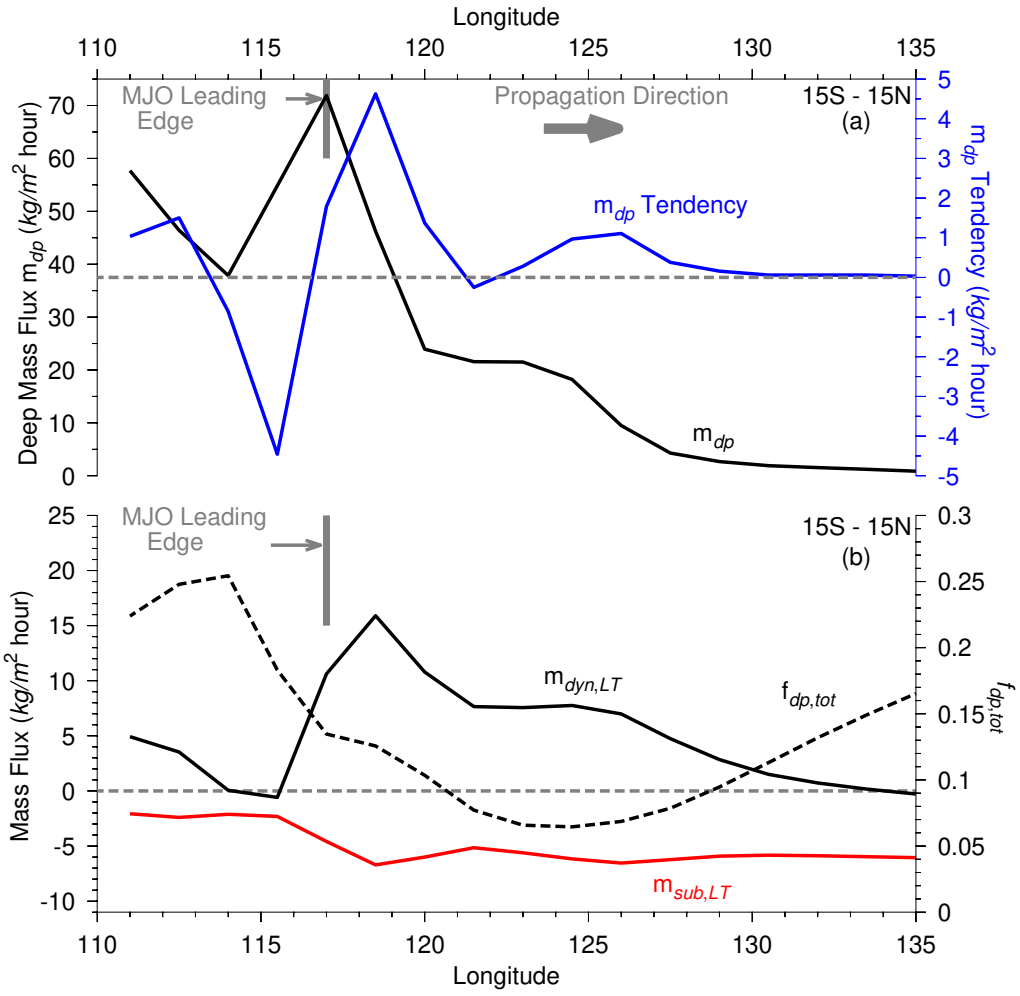

FIG. 16: (a) The top panel shows the zonal variation of the the 15 ^{o}S - 15 ^{o}N deep convective mass flux m_{dp} (black), and the deep mass flux tendency (blue), on both sides of the leading eastern edge of the composite MJO. The leading edge is identified as the longitude of the most eastward squall line of the MJO, or most eastward m_{dp} maximum. The deep mass flux m_{dp} lags the m_{dp} tendency. (b) The lower panel shows the zonal variation of the variables that determine the m_{dp} tendency. The downward lower tropospheric subsidence mass flux (shown in red) is almost independent of longitude. The increase in total upward lower tropospheric mass flux in advance of the MJO is therefore mainly due to the dynamical component $m_{dyn,LT}$, shown in black. The dashed line refers to the $f_{dp,tot}$, which is the product of $f_{dp}(cape_{UT})$ and $f_{dp}(colrh)$. It characterizes the net effect of both upper tropospheric CAPE and column relative humidity on the m_{dp} tendency.

and replace the integral over time with an integral over distance along the equator. If the speed v_{MJO} is constant, we can write

$$v_{MJO} = \frac{\int_{of\,LE}^{east} m_{dp,prod}\,dx}{m_{dp,LE}}. \tag{24}$$

It is understood that the integral extends to the right of the leading edge grid cell. Using the values for $m_{dp,LE}$ and $m_{dp,prod}$ shown in the top panel of Figure 16 gives $v_{MJO} = 5.78$ m/s. This

is reasonably close to the simulated MJO propagation speed $v = 6.43$ m/s. Because the downdraft mass flux and the induced upward ascent from the downdraft circulation can both be expected to be proportional to the deep mass flux, both numerator and denominator in Eq. (24) should be proportional to the deep convective mass flux of the MJO. To first order, the MJO propagation speed should therefore not depend on the MJO amplitude.

In Eq. (21), the production of deep convective mass flux is proportional to the product of the two sigmoidal functions which capture the sensitivity of the deep mass flux tendency to column relative humidity and CAPE, i.e., $f_{dp}(colrh)$ and $f_{dp}(cape_{UT})$. The lower panel of Figure 16 shows the product of the two sigmoidal functions, $f_{dp,tot}$. Upper tropospheric CAPE is usually sufficiently large that $f_{dp}(cape_{UT})$ is reasonably close to 1. The main reason for the smaller values of $f_{dp,tot}$ in advance of the MJO is, therefore, that the column relative humidity is lower than the critical value $colrh_{half} = 0.8$ for $f_{dp}(colrh)$ shown in Figure 7.

The deep convective mass flux production is also proportional to the sum of the dynamical and subsidence vertical mass flux, $m_{dyn,LT} + m_{sub,LT}$. The mean longitudinal variation of these two mass fluxes in the vicinity of the leading edge of the MJO is also shown in the lower panel of Figure 16. The longitudinal variation in the total vertical motion is dominated by the dynamical component, which exhibits a peak one grid cell in advance of the leading edge. The propagation of the MJO can therefore be attributed to the extension of the downdraft congestus circulation outside the direct envelope of the MJO. In the model, one of the reasons for the slow MJO propagation speed is because of the net subsidence between MJO events. MJO events must therefore continuously advance into regions of reduced column relative humidity, within which the $f_{dp,tot}$ factor reduces the efficiency with which net upward lower tropospheric motion can generate new deep convection. Furthermore, in order to produce a net positive deep mass flux tendency in advance of the MJO, the downdraft circulation within the MJO envelope must first produce sufficient upward dynamic motion to exceed the subsidence descent.

6. Discussion

One advantage of the simple and parameterized nature of the model is that the effects of various processes on the behavior of the MJO events simulated by the model can be easily modified by adjusting particular model parameters.

a. Downdraft circulation length scale

In the model, the deep updraft mass flux is roughly twice as large as the downdraft mass flux. In order for the induced lower tropospheric ascent that is part of the downdraft congestus circulation to locally exceed the induced descent from the deep circulation, it is necessary that the ascent be concentrated in a spatially smaller area than the descent. The model would therefore be expected to simulate MJO events only when the downdraft circulation length scale was significantly smaller than the deep updraft length scale (i.e., $L_{LT} < L_{UT}$). The upper panel of Figure 17 shows the Hovmöller rainfall diagram that results when the downdraft circulation length scale is increased from the default $L_{LT} = 500$ km, to $L_{LT} = 700$ km. Rainfall clusters continue to appear at particular fixed latitudes. They grow until they reach a size comparable with an MJO, but then rapidly dissipate and do not propagate. If the downdraft circulation length scale L_{LT} is incrementally increased from its default value, the latitudinal range of the MJO events tends to expand, and the MJO propagation speed slightly decreases. Future increases in tropical tropospheric temperatures will presumably give rise to an upward trend in the height of the melting level (Folkins 2013), and therefore, potential modest increases in the spatial scale of the downdraft congestus circulation.

b. Role of the Zonal Asymmetry Parameter

The lower panel of Figure 17 hows the Hovmöller diagram that results when the zonal asymmetry parameter $f_{L,asym}$ is set to 1. In this case, the horizontal mass transport induced by a local surplus or deficit of mass in a grid box is zonally symmetric. The initiation of westward propagation of the MJO events at day 25 can presumably be attributed to a small bias in the model which favors propagation toward the west. The propagation speed of the simulated MJO events, whether eastward or westward, is essentially independent of the value of $f_{L,asym}$. It can be shown that the effect of $f_{R,asym}$ on the MJO propagation direction is mainly determined by its effect on horizontal transport in the boundary layer. For example, increased horizontal transport in the boundary layer toward an MJO on the western side for $f_{R,asym} < 1$ favors increased downward dynamical and subsidence vertical motion. This would reduce the water vapor mixing ratio of the boundary layer and the congestus and deep convective mass fluxes on the western side, and favor eastern propagation.

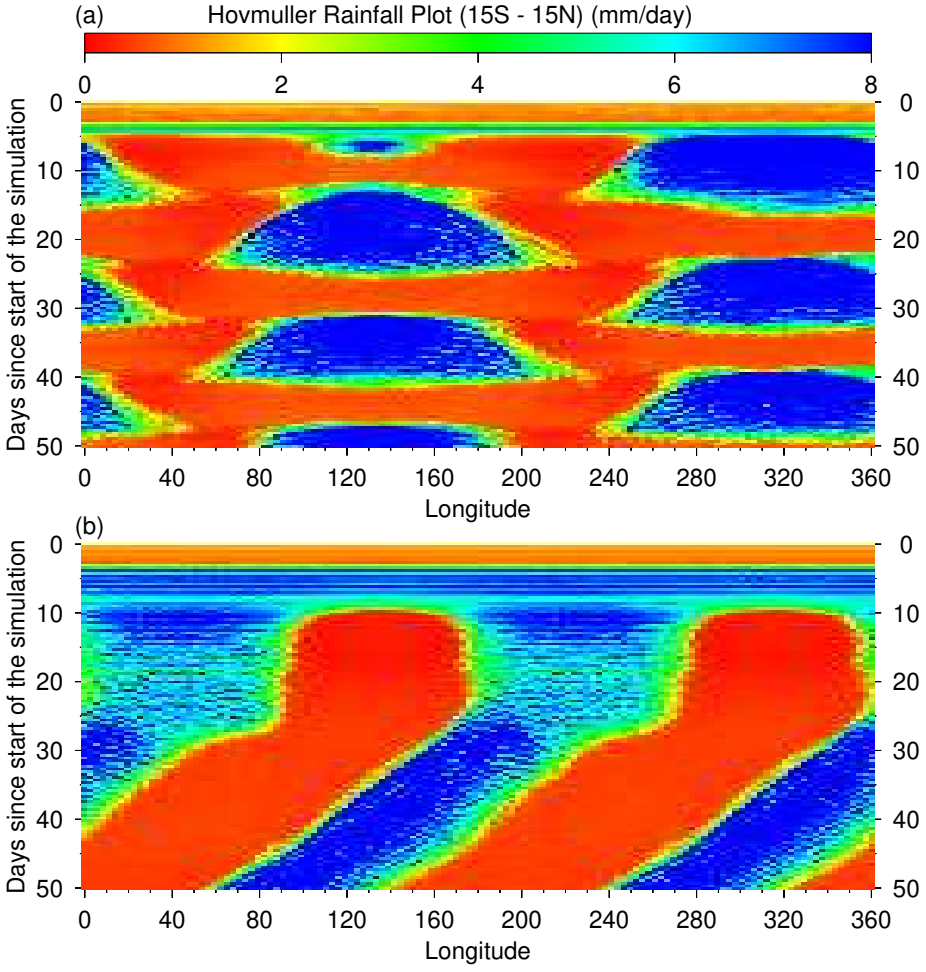

FIG. 17: (a) The top panel shows the Hovmöller diagram of the first 50 days of a model simulation in which the length scale of the downdraft congestus circulation L_{LT} is increased from 500 km to 700 km. (b) The lower panel shows a Hovmöller diagram of the first 50 days of a model simulation in which the zonal asymmetry parameter $f_{L,asym}$ is set to 1, so that the horizontal transport caused by a local mass deficit or excess are symmetric about the eastward and westward directions.

c. Downdrafts

The downdraft mass flux is partially constrained by the amount of deep rainfall available to evaporatively cool lower tropospheric air parcels to a sufficient degree that they have a negative buoyancy when moved downward to the boundary layer. However, the main constraint on the downdraft mass flux is that it is not permitted to be larger than a prescribed fraction of the deep updraft mass flux. This prescribed maximum fraction increases from $f_{dn,min} = 0$ at low m_{dp}, to $f_{dn,add} = 0.8$ at large m_{dp}, with a transition near $m_{dp,half} = 25$ kg/(m^{2}hour). If $f_{dn,add}$ is reduced to 0.6, the model does not exhibit MJO rainfall variance. If $f_{dn,add} = 0.7$, the model continues to exhibit MJO variance, but there are also occasional longitudinal bands of non propagating rainfall.

If the downdraft fraction f_{dn} is fixed at 0.6 or 0.7, rainfall clustering on the spatial scale of an MJO continues to occur, but there is no propagation.

d. Congestus clouds

The congestus mass flux is proportional to the a_{cg} parameter, which determines the strength of the coupling with the lower tropospheric total vertical motion. The MJO variance in the model is considerably weakened if this parameter is reduced from the default value of $a_{cg} = 3$ to $a_{cg} = 1$, and is reduced to zero for $a_{cg} = 0.5$. It is not affected by the deactivation of the parameterization for congestus rainfall evaporation. This suggests that the mechanism by which congestus clouds generate MJO rainfall variance is not exclusively through lower tropospheric moistening.

7. Issues related to the coupling of convective mass fluxes to vertical motion

We have argued that, in constructing a convective parameterization, it is useful to pay particular attention to the interaction between the clear sky vertical motion and the convective mass fluxes. As such, the most useful diagnostic target is the observed variation in the vertical structure of mass divergence during the growth and decay of high rain events shown in Figure 12 (Mitovski et al. 2010). In the model, agreement with this observational target has been achieved through the use of a convective parameterization in which the mid-level congestus mode is in phase with the net background vertical motion, while the tendency of the deep convective mode is in phase with the background vertical motion. This may also be a desirable way to couple convective mass fluxes to grid scale dynamics in models with more realistic dynamics.

The vertical motion that is directly available in climate models is usually the pressure velocity ω that is obtained through imposing mass conservation. As such, it refers to the sum of all vertical mass fluxes arising from both grid scale dynamics and sub grid scale convective motions. However, as shown in Figure 13, even at modest rates of convective precipitation, the net background, or clear sky vertical motion $m_{dyn,LT} + m_{sub,LT}$, in the model is smaller than the updraft and downdraft convective mass fluxes, and can be of opposite sign to the total vertical motion. In a climate model, it may be difficult to determine the background clear sky vertical motion that would be most appropriate to couple to the convective mass fluxes. It would be inappropriate to couple

the convective fluxes directly to the model ω, however, because this would essentially couple the convective mass fluxes to themselves, and generate unrealistic nonlinear feedbacks.

There are other issues which arise from the way convective parameterizations are sometimes formulated in climate models. A convective parameterization usually consists of plumes or parcels that entrain air from the boundary layer, rise vertically under the influence of buoyancy, produce precipitation when saturated, and detrain into the free troposphere when they become negatively buoyant. Net convective detrainment into a grid cell increases the mass of that grid cell. However, above the boundary layer, the top and bottom surfaces of a grid cell are usually defined at fixed pressure levels. Because the convective parameterization must retain hydrostatic balance within a time step, the net upward convective motion of a column must therefore be compensated by immediate descent within the column. When convection is occurring in a model column, outward divergent grid scale flow usually occurs at heights where there is net convective detrainment, and inward convergent grid scale flow occurs where there is net convective entrainment. By mass continuity, convection is therefore usually accompanied by upward grid scale mass transport from heights where there is net entrainment, to heights where there is net detrainment. The descent that occurs within the convective parameterization is therefore largely offset by the ascent that occurs at the grid scale.

However, the excessive and redundant vertical transport that comes from the lack of integration of the convective and grid scale dynamics, so that the enforcement of hydrostatic balance occurs individually for each process, may lead to excessive numerical diffusion in the vertical at higher rates of convective precipitation (Lawrence and Salzmann 2008). This issue may be exacerbated at higher horizontal resolutions, where the simulated rainfall variance and associated vertical motions are likely to be larger. However, it would be alleviated by having a smaller time step, so that there would be a more continuous upward flow of air within the convective parameterization, followed by detrainment and outward grid scale horizontal transport.

In the model used here, excessive unrealistic subsidence within the grid column has been avoided by allowing flexibility in the upper and lower pressure boundaries of a grid cell. Grid cells where detrainment is occurring are permitted to absorb the additional detrained mass without immediate induced subsidence. It has also been alleviated by imposing some representation of immediate outward or inward horizontal transport of some fraction of the local grid cell mass surplus or

deficit. Although these methods may be inappropriate for more realistic climate models, it would likely be desirable to have some way of avoiding the artificially induced subsidence that occurs with some convective mass flux parameterizations.

8. Discussion and summary

The building block model of tropical convection (Mapes et al. 2006; Khouider and Majda 2006) has been implemented in a simplified model of the tropics. In this approach, the main convective heating profiles are considered to be those due to deep, stratiform, and congestus clouds. These basic heating profiles both generate and respond to the background vertical motion. Simulation of tropical rainfall variance requires that these basic building blocks be in correct spatial and temporal alignment with each other, and with the background vertical motion. The building block convective parameterization used here was developed using rawinsonde profiles of mass divergence during the growth and decay of high rain events near the equator as an observational target. The two most important assumptions of the convective parameterization are that, while the congestus mass flux is in phase with the lower tropospheric upward motion, the deep convective mass flux *tendency* is in phase with the vertical motion in the lower troposphere.

Horizontal transport in the model is not directly generated by the pressure gradient and Coriolis accelerations, but is instead constrained by two main assumptions: (1) that the length scale for horizontal transport by the downdraft congestus circulation is roughly half that of the deep circulation, and (2) that the length scales of both circulations decrease with distance from the equator. The enforcement of these two constraints enables the simulation of an eastward propagating rainfall mode that exhibits many of the observed properties of the MJO. These include the propagation speed, internal multiscale structure, horizontal spatial scale, enhanced westerly inflow along the trailing edge, and enhanced cumulus congestus clouds at the leading edge. Higher rainfall rates within the MJO envelope are maintained mainly by increased variance in lower tropospheric vertical motion, and by enhanced column relative humidity.

Forward propagation of the MJO does require, however, that some fraction of the upward motion generated by the downdraft circulation within the MJO propagate ahead of the MJO, and contribute to the net upward motion and growth of the deep convective mass flux in advance of the leading edge. In the model, once a lower tropospheric mass deficit is generated within the MJO by a

downdraft, the generation of new lower tropospheric upward motion in advance of the leading edge is essentially instantaneous. The rate of forward motion of an MJO is therefore mainly constrained by the timescale with which the deep convective mass flux responds to this upward motion. In the model, the efficiency with which net upward motion in the lower troposphere can produce deep convection is a nonlinear function of the column relative humidity. This reduces the MJO propagation speed, because the column relative humidity between MJO events is typically lower than the threshold value required to support significant deep convection. In addition, although this is essentially enforced by fiat in the model, it is also probably necessary that the waves which contribute to the residual upward motion in front of the MJO experience some form of dissipation, since the net vertical motion generated by freely propagating continuous waves integrates to zero over a full period.

In the model, MJO events can only move forward when the downdraft circulations that generate the upward motion in front of the MJO also move forward. This is in contrast with other types of convectively coupled waves, in which the lower tropospheric upward motion that supports the convection is continuously generated by the forward propagation of the wave itself as it interacts with the background atmospheric stability.

The main limitation of the model is that the length scales of the downdraft and deep convective circulations have been hardwired by parameterizations. It would be preferable that these length scales be shown to freely evolve from interactions between the equations of motion and the convective parameterization. This would then potentially allow other forms of convectively coupled waves to be simulated, as opposed to having almost all of the rainfall variance concentrated within a single mode with an unrealistically large power, as occurs in this model. However, the length scales used here for the deep updraft and stratiform downdraft circulations are significantly smaller than those obtained from the expression for the Rossby radius of a heat source based on its latitude and vertical depth. Therefore, depending on the horizontal and vertical resolution of the model, it may be necessary to introduce some form of dissipation, or effective reduced downdraft cooling depth, to reduce the downdraft circulation length scale to a value closer to that used here.

The second limitation of the model is that the horizontal transports used to smooth out local grid cell mass anomalies are assumed to be occur within the one hour time step of the model. This is likely to be reasonably realistic for temperature, which is homogenized in the horizontal by gravity

waves on a time scale of several hours (Sobel et al. 2001), but it is clearly less realistic in the case of tracers such as water vapor whose homogenization requires physical advection.

Acknowledgments. This research was supported by the Natural Sciences and Engineering Council of Canada. The TRMM data were provided by the NASA/Goddard Space Flight Center's Mesoscale Atmospheric Processes Laboratory and PPS, which develop and compute the TMPA as a contribution to TRMM. We thank the Atmospheric Processes And their Role in Climate (APARC) Programme for making the HVRRD high resolution radiosonde data available for the work described in this article. These activities have been undertaken under the guidance and sponsorship of the World Climate Research Programme. Please contact the author for the model source code, or see https://www.mathstat.dal.ca/~folkins/.

References

Bister, M., and B. E. Mapes, 2004: Effect of vertical dipole temperature anomalies on convection in a cloud model. *Journal of the Atmospheric Sciences*, **61**, 2092–2100, https://doi.org/10.1175/1520-0469(2004)061<2092:EOVDTA>2.0.CO;2.

Chen, G., and B. Wang, 2020: Circulation factors determining the propagation speed of the Madden–Julian oscillation. *Journal of Climate*, **33**, 3367–3380, https://doi.org/10.1175/JCLI-D-19-0661.1.

Durre, I., R. S. Vose, and D. B. Wuertz, 2006: Overview of the Integrated Global Radiosonde Archive. *Journal of Climate*, **19**, 53–68, https://doi.org/10.1175/JCLI3594.1.

Folkins, I., 2013: The melting level stability anomaly in the tropics. *Atmospheric Chemistry and Physics*, **13**, 1167–1176, https://doi.org/10.5194/acp-13-1167-2013.

Guichard, F., and F. Couvreux, 2017: A short review of numerical cloud-resolving models. *Tellus A: Dynamic Meteorology and Oceanography*, **69**, https://doi.org/10.1080/16000870.2017.1373578.

Holloway, C. E., and J. D. Neelin, 2009: Moisture vertical structure, column water vapor, and tropical deep convection. *Journal of the Atmospheric Sciences*, **66**, 1665 – 1683, https://doi.org/10.1175/2008JAS2806.1.

Huffman, G. J., E. F. Stocker, D. T. Bolvin, E. J. Nelkin, and R. F. Adler, 2012: TRMM Version 7 3B42 and 3B43 Data Sets. NASA/GSFC, Greenbelt, MD, Dataset accessed at http://mirador.gsfc.nasa.gov/cgibin/mirador/presentNavigation.pl.

Hung, M.-P., J.-L. Lin, W. Wang, D. Kim, T. Shinoda, and S. J. Weaver, 2013: MJO and convectively coupled equatorial waves simulated by CMIP5 climate models. *Journal of Climate*, **26 (17)**, 6185–6214, https://doi.org/10.1175/JCLI-D-12-00541.1.

Inoue, K., Ángel F. Adames, and K. Yasunaga, 2020: Vertical velocity profiles in convectively coupled equatorial waves and MJO: New diagnoses of vertical velocity profiles in the wavenumber–frequency domain. *Journal of the Atmospheric Sciences*, **77**, 2139 – 2162, https://doi.org/10.1175/JAS-D-19-0209.1.

Johnson, R. H., T. M. Rickenbach, S. A. Rutledge, P. E. Ciesielski, and W. H. Schubert, 1999: Trimodal characteristics of tropical convection. *Journal of Climate*, **12 (8)**, 2397–2418, https://doi.org/10.1175/1520-0442(1999)012<2397:TCOTC>2.0.CO;2.

Khouider, B., and A. J. Majda, 2006: Multicloud convective parametrizations with crude vertical structure. *Theor. Comput. Fluid Dyn.*, **20**, 351 – 375, https://doi.org/10.1007/s00162-006-0013-2.

Kiladis, G. N., K. H. Straub, and P. T. Haertel, 2005: Zonal and vertical structure of the Madden–Julian Oscillation. *Journal of the Atmospheric Sciences*, **62**, 2790 – 2809, https://doi.org/10.1175/JAS3520.1.

Lawrence, M. G., and M. Salzmann, 2008: On interpreting studies of tracer transport by deep cumulus convection and its effects on atmospheric chemistry. *Atmos. Chem. Phys.*, **8**, 6037–6050, https://doi.org/doi.org/10.5194/acp-8-6037-2008.

Lin, J.-L., M. Zhang, and B. Mapes, 2005: Zonal momentum budget of the Madden–Julian Oscillation: The source and strength of equivalent linear damping. *Journal of the Atmospheric Sciences*, **62**, 2172 – 2188, https://doi.org/10.1175/JAS3471.1.

Mapes, B., S. Tulich, J. Lin, and P. Zuidema, 2006: The mesoscale convection life cycle: Building block or prototype for large-scale tropical waves? *Dynamics of Atmospheres and Oceans*, **42 (1-4)**, 3–29, https://doi.org/10.1016/j.dynatmoce.2006.03.003.

Mapes, B. E., 1993: Gregarious tropical convection. *Journal of the Atmospheric Sciences*, **50**, 2026–2037, https://doi.org/10.1175/1520-0469(1993)050<2026:GTC>2.0.CO;2.

Mapes, B. E., and R. A. Houze, 1995: Diabatic divergence profiles in Western Pacific mesoscale convective systems. *Journal of the Atmospheric Sciences*, **52**, 1807 – 1828, https://doi.org/10.1175/1520-0469(1995)052<1807:DDPIWP>2.0.CO;2.

Mitovski, T., I. Folkins, R. V. Martin, and M. Cooper, 2012: Testing convective transport on short time scales: Comparisons with mass divergence and ozone anomaly patterns about high rain events. *Journal of Geophysical Research: Atmospheres*, **117 (D2)**, https://doi.org/10.1029/2011JD016321, https://agupubs.onlinelibrary.wiley.com/doi/pdf/10.1029/2011JD016321.

Mitovski, T., I. Folkins, K. von Salzen, and M. Sigmond, 2010: Temperature, relative humidity, and divergence response to high rainfall events in the tropics: Observations and models. *Journal of Climate*, **23 (13)**, 3613–3625, https://doi.org/10.1175/2010JCLI3436.1.

Ren, P., D. Kim, M.-S. Ahn, D. Kang, and H.-L. Ren, 2021: Intercomparison of MJO column moist static energy and water vapor budget among six modern reanalysis products. *Journal of Climate*, **34**, 2977–3001, https://doi.org/10.1175/JCLI-D-20-0653.1.

Sherwood, S. C., and R. Wahrlich, 1999: Observed evolution of tropical deep convective events and their environment. *Monthly Weather Review*, **127**, 1777–1795, https://doi.org/10.1175/1520-0493(1999)127<1777:OEOTDC>2.0.CO;2.

Sobel, A. H., J. Nilsson, and L. M. Polvani, 2001: The weak temperature gradient approximation and balanced tropical moisture waves. *Journal of the Atmospheric Sciences*, **58 (23)**, 3650–3665, https://doi.org/10.1175/1520-0469(2001)058<3650:TWTGAA>2.0.CO;2.

Virman, M., M. Bister, V. A. Sinclair, J. Räisänen, and H. Järvinen, 2020: Vertical temperature structure associated with evaporation of stratiform precipitation in idealized WRF simulations. *Journal of the Atmospheric Sciences*, **77**, 1851–1864, https://doi.org/10.1175/JAS-D-19-0111.1.

Waite, M. L., and B. Khouider, 2010: The deepening of tropical convection by congestus preconditioning. *Journal of the Atmospheric Sciences*, **67**, 2601 – 2615, https://doi.org/10.1175/2010JAS3357.1.

Wheeler, M., and G. N. Kiladis, 1999: Convectively coupled equatorial waves: Analysis of clouds and temperature in the wavenumber–frequency domain. *Journal of the Atmospheric Sciences*, **56 (3)**, 374–399, https://doi.org/10.1175/1520-0469(1999)056<0374:CCEWAO>2.0.CO;2.

Windmiller, J. M., J. Bao, S. C. Sherwood, T. D. Schanzer, and D. Fuchs, 2023: Predicting convective downdrafts from updrafts and environmental conditions in a global storm resolving simulation. *Journal of Advances in Modeling Earth Systems*, **15**, https://doi.org/10.1029/2022MS003048.

Zhang, C., A. F. Adames, B. Khouider, B. Wang, and D. Yang, 2020: Four theories of the Madden-Julian Oscillation. *Reviews of Geophysics*, **58**, 1–55, https://doi.org/10.1029/2019RG000685.